THESIS FOR THE DEGREE OF DOCTOR OF PHILOSOPHY

Dark matter electron interactions in detector materials

Einar Urdshals

Department of Physics
Chalmers University of Technology
Gothenburg, Sweden, 2024

Dark matter electron interactions in detector materials

Einar Urdshals

ISBN 978-91-8103-031-0

Acknowledgements, dedications, and similar personal statements in this thesis, reflect the author's own views. Parts of the thesis is reused from the licentiate thesis by the same author in accordance with the rules at Chalmers. The front page image has been created with DALL · E 2.

Doktorsavhandlingar vid Chalmers tekniska högskola, Ny serie nr 5489
ISSN 0346-718X This thesis has been prepared using LaTeX.

Department of Physics
Chalmers University of Technology
SE-412 96 Gothenburg, Sweden
Phone: + 46 (0)31-772 1000
www.chalmers.se

Printed by Chalmers Digitaltryck
Gothenburg, Sweden, March 2024

Dark matter electron interactions in detector materials
Einar Urdshals, Department of Physics
Chalmers University of Technology

Abstract

Dark Matter (DM) makes up 85% of the matter content of the universe, and its gravitational effects are seen on scales ranging from that of cosmology to that of galactic astrophysics. The nature of DM is, however, unknown. Studying DM in the lab with a class of experiments called direct detection (DD) experiments is key to understanding its properties. For decades, experiments have been attempting to do this through searches for DM induced nuclear recoils. These have not been found, and a possible reason for this is that the hypothetical DM particle is too light to induce nuclear recoils. Therefore, in the last decade experiments have been built to study DM through electron recoils instead. As the electron is 4 orders of magnitude lighter than the nucleus, electron recoils can be induced by DM down to 4 orders of magnitude lighter than the lightest DM particle probeable with nuclear recoils.

In order to understand current and upcoming results from experiments searching for DM induced electron recoils, a theoretical understanding of DM electron scatterings in detector materials is needed. When modelling such electron interactions, one need input both from DM and material physics.

This thesis improves the theoretical understanding by both improving the material description using density functional theory (DFT), and by extending the DM description using non-relativistic effective theory (NR-EFT) tools. The improvement gives not only a more accurate description of the DM-electron interactions that the experiments are expected to see; it also vastly extends the forms of DM that can be studied in direct detection experiments. Before this extension, one typically focused on a benchmark case of DM, the so called dark photon model. With this extension, one can cover all forms of gravitationally bound DM with spins of 0, 1/2 or 1.

In the included works, advances are made in the description of DM-electron interactions in common detector materials such as liquid xenon, silicon and germanium, as well as to materials in the research and development phase, such as graphene and carbon nanotubes (CNTs).

Keywords: Dark matter, direct detection, effective theory

To Jasmina.

List of Publications

Publications Included in this Thesis

1. R. Catena, T. Emken, M. Matas, N. A. Spaldin, and E. Urdshals, "Crystal responses to general dark matter-electron interactions," *Phys. Rev. Res.*, vol. 3, no. 3, p. 033 149, 2021

2. R. Catena, D. Cole, T. Emken, M. Matas, N. Spaldin, W. Tarantino, and E. Urdshals, "Dark matter-electron interactions in materials beyond the dark photon model," *JCAP*, vol. 03, p. 052, 2023

3. R. Catena, T. Emken, M. Matas, N. A. Spaldin, and E. Urdshals, "Direct searches for general dark matter-electron interactions with graphene detectors: Part I. Electronic structure calculations," *Phys. Rev. Res.*, vol. 5, no. 4, p. 043 257, 2023

4. R. Catena, T. Emken, M. Matas, N. A. Spaldin, and E. Urdshals, "Direct searches for general dark matter-electron interactions with graphene detectors: Part II. Sensitivity studies," *Phys. Rev. Res.*, vol. 5, no. 4, p. 043 258, 2023

5. R. Catena, L. Marin, M. Matas, N. A. Spaldin, and E. Urdshals, "Density-functional theory description of xenon for light dark matter direct detection," (In preparation)

6. R. Catena and E. Urdshals, "Dark Matter-induced electron excitations in silicon and germanium with Deep Learning," Mar. 2024

Other Publications not Included in this Thesis

F. Kahlhoefer and E. Urdshals, "On dark atoms, massive dark photons and millicharged sub-components," *Phys. Lett. B*, vol. 807, p. 135 601, 2020

Statement of Contributions

1. In Paper 1, I developed most of the theoretical framework, developed the code and ran the numerical calculations and analysis, and wrote parts of the text.

2. In Paper 2, I provided support with using the code developed in Paper 1, and made figures 1 and 2.

3. In paper 3, I developed parts of the theoretical framework and the code, and ran the numerical calculations and analysis. I also wrote parts of the text.

4. In paper 4, I developed parts of the theoretical framework and the code, and ran the numerical calculations and analysis. I also wrote parts of the text.

5. In paper 5, I developed parts of the theoretical framework and the code, and ran some of the numerical calculations and analysis. I also wrote parts of the text.

6. In paper 6, I developed the needed computer codes, developed the necessary framework and wrote the first version of the paper.

Acknowledgments

Firstly, I would like to thank Riccardo for his careful, detailed and generous supervison. Your door is always open, and I have truly learned a lot from our many physics discussions. Your width of knowledge and ability to grasp and reason about a wide variety of topics never cease to amaze me.

To Timon, Hanna, Daniel, Nicola, Marek and Luca: Thank you for your fruitful collaboration. Timon for his rigorous work, and caution against juumping to conclusions. Hanna for many discussions and great insight into computation, it was a pleasure to co-supervise you! Daniel for his quick understanding and thorough work on the physics of dark matter electron interactions. Nicola, Marek and Luca for teaching me a lot about the amazing physics of solids and fluids, a field I had little experience with before starting my PhD. Our several meetings and discussions have truly been a pleasure!

To Taylor: Thanks for many fun chats in the office!

To Eric, Oliver, Michal, Sean, Isak, Tor, Joakim, Alexandra, Matthias, Avik, Hans, Chirstian, Gabriele, Andreas, Andreas, Ulf, Björn, Martin, Bengt, Simone and many more: Thanks for making my time at Chalmers memorable!

Lastly, to Øystein, Magnhild and Jill: Thanks for sparking my fascination with physics!

Acronyms

AGN:	Active Galactic Nucleus
ALP:	Axion Like Particle
AI:	Artificial Intelligence
CMB:	Cosmic Microwave Background
CNT:	Carbon NanoTube
CP:	Charge-conjugation Parity
DD:	Direct Detection
DFT:	Density Functional Theory
DM:	Dark Matter
EFT:	Effective Field Theory
FFNN:	FeedForward Neural Network
GGA:	Generalized Gradient Approximation
GW:	Gravitational Waves
ISM:	InterStellar Medium
LSD:	Local Spin Density
LSS:	Large Scale Structure
NN:	Neural Network
NR-EFT:	Non-Relativistic Effective Field Theory
PBH:	Primordial Black Hole
QCD:	Quantum Chromodynamics
QFT:	Quantum Field Theory

SD:	Spin Dependent
SHM:	Standard Halo Model
SI:	Spin Independent
SM:	Standard model
WIMP:	Weakly Interacting Massive Particle

Contents

Part I

Overview

CHAPTER 1

Introduction

In modern physics, the mystery of dark matter (DM) is one of the most fundamental and fascinating problems yet to be solved. On the one hand the effects of the gravitational pull of DM on visible matter such as electrons and protons in the universe implies that DM makes up 85% of the matter content of the universe [1]. On the other it is still unknown what DM is made of.

The gravitational effects of DM are seen on several scales, and play a crucial role in understanding the universe. Shortly after the Big Bang, while the visible matter exists in the form of a plasma, it is being kept from clumping due to the photon radiation pressure. In contrast, a defining feature of DM is that it couples weakly to the photon, and is therefore free to clump together and form gravitational wells that pull on the visible matter[1]. These wells give rise to over- and underdensities of visible matter, which has been observed in the cosmic microwave background by WMAP [2] and Planck [3]. The gravitational wells formed by DM do not only play a role in shaping the cosmic microwave background; they are also crucial in structure formation, the process in which cosmological structures such as galaxies form around these

[1] In fact the visible matter density oscillates around these wells, a phenomenon called Barion Acoustic Oscillations.

gravitational wells. Both the origin of the cosmic microwave background and the structure formation of galaxies is well described and understood by the ΛCDM[2] model, also known as the Standard Model of Cosmology. The success of ΛCDM, a model in which DM is a key component, is strong evidence for the existence of DM.

The gravitational effect of DM is not only seen on cosmological scales, but also on the scales of galaxy clusters, galaxies and dwarf galaxies. It was first observed on these scales through the comparison of the velocity dispersion of the galaxies in the Coma cluster with the visible mass contained in the stars in these galaxies. The comparison showed that there had to be invisible dark matter in addition to the glowing stars in order to provide enough gravitational pull to produce the observed velocities [4]. Later, one has more systematically mapped velocities of stars and other visible objects such as hydrogen clouds as a function of distance from the center of galaxies in what is known as galactic rotation curves[3]. Today, rotation curves are used to infer DM density distributions in galaxies, information which is a valuable input in experiments to detect DM, and which is used to obtain the results in the papers on which this thesis builds.

There is a large number of candidates for DM. A notable one is primordial black holes (PBH) [5]; black holes formed in the early universe which remain until today. This is an attractive candidate as it does not require new physics. Within general relativity, PBH can be formed as a result of over densities in the early universe, and would survive until today as long as the mass is larger than $10^{15}\,\mathrm{g}$[4]. There are however multiple expected effects of PBH, such as destruction of neutron- and dwarf stars and lensing effects of PBH passing between Earth and distant stars which one does not observe. Due to this lack of observation it now seems unlikely that PBH can constitute all of DM [8], although it is still possible that PBH can make up some of the DM. This possibility will be further clarified by the recent breakthrough in observations

[2] Λ here refers to the cosmological constant, whereas CDM stands for Cold Dark Matter. These are the two ingredients that need to be added to standard particle physics and general relativity to correctly predict the cosmic microwave background and the details of structure formation.

[3] Galactic rotation curves are plots of the velocity of visible objects such as stars, and more recently hydrogen clouds, as a function of their distance to the center of the galaxy. From this the mass distribution within the galaxy can be inferred.

[4] Black holes evaporate due to Hawking radiation [6], [7], and the lower mass limit of $10^{15}\,\mathrm{g}$ is easily obtained knowing the physics of Hawking radiation and the age of the universe. It is stated in ref. [5], published the year after the first publication on Hawking radiation.

of gravitational waves (GW) by the Ligo and Virgo collaborations [9], and upcoming space based experiments are expected to measure GW with even greater sensitivity. They would be able to detect GW emitted from mergings of PBH with each other or with compact objects such as neutron stars, thereby shedding more light on a possible population of PBH.

Another possibility[5] is that DM is made up of particles, which will be the underlying hypothesis of this thesis. As there is no particle in the Standard Model of Particle Physics (SM) that can constitute DM[6], new physics is needed and the number of proposed models of DM particles is vast. The most popular is the Weakly Interacting Massive Particle (WIMP), a massive particle which interacts with the SM via the weak force. The reason for the popularity of WIMPs is (in addition to its simplicity) the so called WIMP miracle; the annihilation cross section needed to create the measured amount of DM from equilibrium with the SM particles in the early universe, is comparable with that of the weak interaction known from the SM. This mechanism of DM creation is known as the freeze-out mechanism[7], as the DM particles are in equilibrium with the SM particles while the universe is sufficiently dense and warm, before leaving equilibrium (freezing out) as the universe expands and cools down at a rate larger than the WIMP annihilation rate.

The axion is another popular DM candidate, a particle which was initially introduced to solve a different problem in particle physics, namely the strong CP problem[8]; Quantum Chromo Dynamics (QCD) seems to be accidentally symmetric under simultaneous charge-conjugation (C) and parity (P) transformations. A proposed explanation for this symmetry is that the CP symmetry corresponds to the ground state of a new field [11], [12], which was later realised to correspond to a new particle with the properties of DM [13], [14].

[5] A third possible explanation of the phenomena typically explained by DM is Modified Newtonian Dynamics[10], in which the Newtonian laws of motion are modified to fit galactic rotation curves.

[6] There is no standard model particle which both has a life-time longer than the age of the universe, interacts weakly enough with light and is heavy enough that it can form the gravitational wells in the early universe.

[7] Another popular and more recently proposed mechanism for DM production in the early universe is known as freeze-in. In this scenario DM never interacts strongly enough with the SM particles for it to be in equilibrium with the SM, but it still interacts strongly enough with the SM that energy leaks from the thermal bath of the SM into that of DM.

[8] In fact the name axion comes from a laundry detergent, since the axion was introduced to clean up the strong CP problem.

The sterile neutrino [15] is yet another DM candidate with the added benefit of solving an additional problem in physics, namely the neutrino mass problem; in the SM neutrinos are massless particles, but phenomena such as neutrino oscillation [16], [17] require the neutrino to have a small, but non-zero mass. This small neutrino mass can be explained by the seesaw mechanism by which the smallness of the neutrino mass is the consequence of the comparatively large mass of the hypothesized sterile neutrino [18].

The candidates for particle DM mentioned above have in common that they interact with each other and the particles of the SM not just gravitationally, but also through other forces. In fact, DM self-interaction might alter the DM distribution in galaxies by DM particles colliding and forming a core in contrast to the cusp like profile expected from non-interacting DM. The DM density profiles expected from self-interaction seem to fit observations better than the ones expected from collisionless DM [19], [20], suggesting DM indeed has non-gravitational interactions and motivating experiments to detect them.

Numerous experiments have been carried out to observe these hypothesised non-gravitational DM interactions with the SM. These experiments fall into 3 categories. The first is that of indirect detection experiments. Several DM models, such as the WIMPs, have the feature that pairs of them can annihilate into highly energetic SM particles. If this happens in or near our galaxy, these SM particles might reach earth and be detected. There is a wide range of experiments searching for such particles. Experiments such as DAMPE, Fermi-LAT, H.E.S.S. search for gamma rays [21]–[23] and cosmic rays[9] [24]–[26], whereas others are dedicated gamma ray experiments such as MAGIC [27] and VERITAS [28], or cosmic ray experiments such as AMS-02 [29]. In addition to gamma rays and cosmic rays there are also experiments searching for neutrinos, such as IceCube [30], ANTARES [31] and KM3NET [32]. These search for neutrinos interacting with water molecules, the first in the Antarctic ice, and latter two in the sea.

Another category is that of particle collider experiments, which work on the opposite principle of the indirect detection experiments. Rather than having DM particles annihilate into SM particles, one accelerates SM particles to very high energies and collide them to produce new particles, hoping some of them might be candidates for DM. In these experiments one looks for missing

[9] Cosmic rays are highly energetic charged particles such as electrons, protons and their anti particles.

transverse momentum, i.e. missing momentum carried away by DM particles after the momentum of all the detectable SM particles has been accounted for. The most notable of these particle colliders is the LHC. It accelerates protons to energies of several TeV, which lead to the discovery of the Higgs boson in 2012 [33]–[35]. Other examples include the Tevatron, known for discovering the top quark [36]–[38], and Belle[10] [39].

The third category is that of direct detection (DD) experiments, the experimental category this thesis will focus on. Such experiments search for energy and momentum deposited by DM in detector materials on earth. Compared to the method of indirect detection mentioned above, DD has the advantage that the interaction between DM and visible matter happens in the lab on earth. This makes it easier to control the environment in which the physics happens and reducing uncertainties from the DM density profile along the line of sight, and from the physics of propagation of charged annihilation products in the galactic magnetic field. The observable deposition of energy and momentum can either happen through absorption of the DM particle, i.e. the mass energy of the DM particle is deposited in the detector, or through elastic scattering, i.e. (parts of) the kinetic energy of the DM particle is deposited. Detection of axions fall in the former category, whereas WIMPs and sterile neutrinos fall in the latter. So far the direct detection community has mostly focused on the detection of WIMPs, and designed experiments with this purpose. WIMPs are expected to have a mass range suitable for depositing energy to nucleus[11], causing the nucleus to recoil. Several experiments are built to search for these nuclear recoils, and their characteristics depend on whether they use solid or liquid detector materials. The liquid detectors mostly use noble gasses such as liquid xenon for XENON1T [41], XENONnT [42], LUX [43] and LZ [44], and liquid argon for Darkside50 [45] and DEAP-3600 [46]. The advantage of liquid detector materials is that they are easy to scale up, allowing experiments with tons of detector material.

Solid target experiments, on the other hand, operate various crystals as detector materials and are much smaller than their liquid counterparts, with typical masses ranging from grams to a few kilograms. They do however op-

[10] Unlike LHC and Tevatron which collides protons with each other, Belle collides electrons with positrons.

[11] The WIMP mass is expected to range from 2 GeV to 100 TeV [40], and for kinematical reasons energy transfer in elastic scatterings lose efficiency when the DM mass differs from the target mass. Considered target masses range from light nucleus like that of oxygen with a mass of 16 GeV to 134 GeV for xenon nucleus.

erate with a smaller energy threshold, making them better suited to probe lower DM masses. Notable experiments in this category are CRESST-III [47] using crystals of $CaWO_4$ as detector material, SENSEI [48] and DAMIC [49] using silicon crystals, EDELWEISS [50] using germanium crystals, and SuperCDMS [51] using both silicon and germanium crystals. Finally, there is a number of experiments using NaI crystals; COSINE [52], COSINUS [53], ANAIS [54], SABRE [55] and DAMA [56]. The latter of these experiments report a scintillation signal with characteristics of DM induced nuclear recoils; it is reported to have the cosine shape with a maximum at June 2nd and minimum at December 2nd expected from yearly modulation[12]. As such, DAMA reports to be seeing evidence of non-gravitational DM interaction, but the report of DAMA is controversial as none of the other above-mentioned collaborations see a similar signal[13].

As there is no decisive evidence for DM induced nuclear recoils despite tremendous experimental efforts, the DD community has started turning their attention towards DM induced electron recoils. Electrons have the advantage of being much lighter than the nucleus, and are therefore suitable for probing much lower DM masses[14] than what is feasible with nuclear recoils. If DM for instance has a mass in the MeV-GeV range, electron recoil experiments might hold the key to the first direct detection of DM particles from our galaxy. An increased theoretical understanding of these DM induced electron recoils will be the main contribution of this thesis. Most of the above mentioned DD experiments, although tailored for nuclear recoils, are also sensitive to electron recoils. XENON1T did interestingly see an unexplained electron recoil spectrum [57] explainable with DM, although this has later been excluded by XENONnT [58], another xenon based experiment. The likely culprit was unaccounted for tritium contamination.

In general, DD experiments struggle to distinguish DM signals from unidentified background sources. A way to mend this is to utilize the directionality

[12] When the orbital velocity of Earth is maximally aligned with the velocity of the Sun relative to the galaxy, the velocity of Earth through the DM halo is at it's highest. At this time the incoming DM flux and velocity is maximal. Six months later the situation is the opposite and the DM flux and velocity is minimal. This modulation is useful as it allows for distinguishing DM signals from constant backgrounds.

[13] The purpose of ANAIS, COSINE, COSINUS and SABRE is largely to crosscheck the result of DAMA with the same detector material to rule out effects from different detector materials.

[14] Electron recoils can be induced by DM masses down to the electron mass, i.e. $\sim 0.5\,\mathrm{MeV}$.

of DM; seem from a lab on Earth, the velocity distribution of incoming DM particles is highly anisotropic. Furthermore, this anisotropic velocity distribution is rotated throughout the day as the Earth rotates, an effect called daily modulation. The velocity distribution does primarily have two important peaks. The best established one is due to the motion of the sun through the solar system, leading to a "headwind" of DM particles. A more recently discussed effect is that of "solar reflection" [59]–[62]: DM particles from the milky way can scatter and get accelerated by energetic particles in the sun, producing a small flux of high energy DM coming from the sun. DD experiments attempting to utilize the anisotropies of the DM velocity distribution are currently in the research and development phase, with notable examples relevant to this thesis is PTOLEMY [63] and ANDROMEDA [64]. These experiments are based on graphene and carbon nanotubes (CNTs), respectively. Graphene and CNTs are anisotropic materials, and therefore have a response which is sensitive to the direction of the DM particle. They would attempt to detect an anisotropic signal with a daily modulation. This very unique signature is not shared with background sources.

In order to understand the DM induced electron recoils, modelling of DM interacting with electrons bound in materials is needed [65]–[69]. Since the non-gravitational interaction (if any) DM has with electrons is unknown, it is important to stay as general as possible. We model the interaction without making assumptions on its form for the first time by employing the framework of non-relativistic effective field theory (NR-EFT): It can be shown that for non-relativistic particles[15] all Galilean invariant interactions can be written in terms of a a finite number of effective operators [70]. The number of such operators is given as $4+20j_\chi$ [71][16], where j_χ is the spin of the DM particle. In practice, interactions described by all possible combinations of these effective operators need to be modelled in realistic detector materials. Focusing on the operators relevant to spin 0 and spin 1/2 DM, we do this for the first time for silicon and germanium crystals in Paper 1 using a state-of-the-art density functional theory (DFT) calculation to accurately capture the crystal

[15] One of the few known properties of DM is that it is gravitiationally bound to the galaxy, and thus that it follows Keplerian motion with a velocity of $\sim 10^{-3}c$. The electron in the target material have a velocity of $\sim Z_{\text{eff}}\,\alpha$, and for the outermost electrons in an atom $Z_{\text{eff}} \sim 1$.

[16] You get $4+20j_\chi$ operators if you include all operators up to and including second order in the DM velocity and the transferred momentum. We do, however, only include operators up to and including first order in the DM velocity, leading to slightly fewer operators.

physics. With the framework we develop and provide, the rate at which DM is expected to produce electron hole pairs in silicon and germanium crystals is easily computed. This expected rate allows for interpretation of the data from experiments such as SENSEI, SuperCDMS and EDELWEISS.

In Paper 2, we demonstrate the importance of the NR-EFT approach using the DFT calculation from Paper 1 together with results for atomic xenon from [72] to calculate the limits silicon, germanium and xenon based DD experiments place on a set of simplified models of DM. These models include scalar, vector and fermionic DM, and shows how one generically gets several contributing effective operators different from the operator usually studied in the benchmark model; the dark photon model.

In Paper 6, we train Neural Networks (NNs) to take a set of effective coupling constants and a DM mass as input, and output rates of electron hole creation in Silicon and Germanium. The NN can compute the same quantities as were computed in Paper 1, but does so many orders of magnitude faster, and does not require the outputs from the DFT calculation. Faster evaluation of the rates of electron hole creation is important if one wants to perform parameter scans, and not needing the DFT outputs makes the NN easier to download and use than the software from Paper 1.

In Papers 3 and 4, we compute the rate of DM induced electron ejections from graphene and CNTs. We imporve the state of the art modelling both by employing DFT to model DM electron scattering in these materials for the first time, and we extend the range of DM models that can be considered using NR-EFT. These papers provide valuable insight into the sensitivities of various detector setups, and forecasts what graphene and CNT based experiments can expect to see. As such, these papers help guide the development of these two future experiments.

Finally, in paper 5, we employ DFT to model liquid Xenon for the first time, allowing us to go beyond the isolated atom description of liquid Xenon. Crucially, we find that the liquid phase shifts and broadens the energy levels of the 5p electrons, leading to a drastic increase in the expected DM induced rate of single and few electron ionizations. This not only strengthens the current exclusion bounds on DM from liquid Xenon, but it also shows that there is more to be gained from lowering the experimental threshold than previously thought.

These works, together with ref. [72], establish NR-EFT in the context of

DM-electron scattering. It shows how going beyond the dark photon model generically reveals new physics with materials reacting in novel ways. In addition, the works improve the state of the art modelling of the material properties relevant to DM electron scattering. As such, they are valuable contributions both to theorists interpreting experimental results, and to experimentalists designing the next generation of experiments.

CHAPTER 2

Evidence for Dark Matter

Dark Matter (DM) is a key ingredient in cosmology as well as galactic and extragalactic astrophysics. Without the gravitational pull it provides several observations cannot be explained. In this chapter cosmology, galactic and extragalactic astrophysics will be reviewed with an emphasis on the impact of DM.

2.1 Cosmology

Below, the evidence for DM in cosmology will be discussed. First, a review of the Standard Model of Cosmology will be given, in which the abundance of dark matter is a free parameter. We will then see that the value of this parameter can be inferred by comparing measurements of the Cosmic Microwave Background (CMB) with simulations based on general relativity and hydrodynamics. We will see that there must be around 5 times as much dark matter as ordinary matter for the simulations to match the observations.

The Standard Model of Cosmology

In the beginning the inflaton created a thermal bath of particles. Now the bath was formless (homogeneous) with the exception of some very small density perturbations.

The Friedmann model describes an expanding homogeneous universe. It is given by the FLRW[1] metric,

$$\mathrm{d}s^2 = -\mathrm{d}t^2 + a^2(t)\left[\frac{\mathrm{d}r^2}{1-kr^2} + r^2\left(\mathrm{d}\theta^2 + \sin^2\theta\,\mathrm{d}\phi^2\right)\right], \tag{2.1}$$

where k is the spatial curvature parameter, and equals 0 for a flat universe. t is the cosmological time, i.e. the time of an observer who sees the universe as being homogeneous[2]. r, θ and ϕ are the spherical comoving coordinates, meaning that they are constant in time and do not expand together with the universe. The time dependence is absorbed in $a(t)$, the scale factor, which increases with time as the universe expands. The Friedmann law can be derived from the Einstein equation, and it governs the time evolution of a:

$$H^2 \equiv \left(\frac{\dot{a}(t)}{a(t)}\right)^2 = \frac{8\pi G}{3}\rho - \frac{k}{a^2} + \frac{\Lambda}{3}, \tag{2.2}$$

with H being the Hubble rate, G being the Newtonian constant of gravitation, ρ being the energy density, Λ being the cosmological constant and $\dot{a}$ denoting the time derivative of a. From the Bianchi identities it can be shown that energy conservation implies that

$$\dot{\rho} = -3\frac{\dot{a}}{a}(\rho + p), \tag{2.3}$$

with p being the pressure. This relation holds for the total energy of the universe, and for decoupled species. One can distinguish between radiation (here taken to be any particle for which $E \gg m$, with E being the energy of the particle and m being the mass) and matter (here taken to be any particle for which $E \approx m$). Matter is pressureless ($p \approx 0$) and radiation has a pressure

[1] The metric is named after Alexander Friedmann, Georges Lemaître, Howard P. Robertson, and Arthur Geoffrey Walker.

[2] The frame in which the universe is homogeneous is the frame in which the cosmic fluid is at rest.

of $p \approx \frac{\rho}{3}$. From the above energy conservation equation it then follows that

$$\rho_m \propto a^{-3}\,, \qquad\qquad \rho_r \propto a^{-4}\,, \tag{2.4}$$

where ρ_m is the density of matter and ρ_r is the density of radiation, with the total density $\rho = \rho_m + \rho_r$. This result can be intuitively understood; The volume of the universe grows as a^3, and for a fixed number of matter particles in a changing volume the density is inversely proportional to the volume. Radiation also gets diluted by the increasing volume just like the matter particles, and in addition it gets red-shifted. As radiation energy is inversely proportional to the wave-length, and the wave-length increases proportionally to a, the radiation volume gets diluted with an additional a^{-1}.

The Friedmann Law thus contains terms proportional to a^{-4} (radiation), a^{-3} (matter), a^{-2} (curvature) and a^0 (cosmological constant Λ), each of which can dominate for different values of a. For small a one can have radiation domination, then matter domination, then curvature domination and finally Λ domination. To make this clearer, the concept of critical densities can be introduced;

$$\rho_c \equiv \frac{3H^2}{8\pi G}\,, \qquad\qquad \rho_c^0 \equiv \frac{3H_0^2}{8\pi G}\,, \tag{2.5}$$

with ρ_c being the critical density and ρ_c^0 (H_0) being the critical density (Hubble rate) today. From this the Ω parameters can be defined:

$$\begin{aligned} \Omega_m &\equiv \frac{\rho_m^0}{\rho_c^0} = \frac{\rho_b^0}{\rho_c^0} + \frac{\rho_{\rm DM}^0}{\rho_c^0} \equiv \Omega_b + \Omega_{\rm DM}\,, \\ \Omega_r &\equiv \frac{\rho_r^0}{\rho_c^0}\,, \quad \Omega_k \equiv \frac{-k}{a_0^2 H_0^2}\,, \quad \Omega_\Lambda \equiv \frac{\Lambda}{3H_0^2}\,, \end{aligned} \tag{2.6}$$

with a_0, ρ_b^0 and $\rho_{\rm DM}^0$ being the value of a and the density of baryons[3] and DM

[3]The mass density of the leptons is negligible.

today respectively. Inserting this in eq. (2.2), it becomes

$$\frac{H^2}{H_0^2} = \left[\Omega_r \left(\frac{a_0}{a}\right)^4 + \Omega_m \left(\frac{a_0}{a}\right)^3 + \Omega_k \left(\frac{a_0}{a}\right)^2 + \Omega_\Lambda\right] , \tag{2.7}$$

$$\frac{H^2}{H_0^2} = \left[\Omega_r \left(1+z\right)^4 + \Omega_m \left(1+z\right)^3 + \Omega_k \left(1+z\right)^2 + \Omega_\Lambda\right] , \tag{2.8}$$

where z is the cosmological redshift, i.e. the redshift of photons between t and today due to the expansion of the universe. Today $H = H_0$, $a = a_0$ and $z = 0$, so the Friedmann equation reads

$$1 = \Omega_r + \Omega_m + \Omega_k + \Omega_\Lambda \, . \tag{2.9}$$

As such Ω_i can be interpreted as the fractions of the total energy of the universe in form i, and the above equation is often referred to as the budget equation.

Cosmic Microwave Background

When the universe is warm, with a temperature larger than the ionization energy of hydrogen, the baryons and electrons in the universe constitute a plasma through which photons cannot propagate freely. As it cools down to a temperature of around 0.26 eV the electrons recombine with the protons to form neutral hydrogen, allowing the thermal photons to propagate freely. These photons then travel through the expanding universe, get red-shifted by a factor of $z_* = 1090$, and arrive at earth from all directions with a temperature of 2.3×10^{-4} eV. They have the spectrum of a black body, and the temperature of photons coming from different directions have small relative variations[4] of 10^{-5}. These variations can be described by a multipole expansion[5] with

[4] Somewhat counter intuitively, the regions of the sky that appear the warmest are in fact the coldest. This is known as the integrated Sachs-Wolfe effect [73], and is due to warmer regions having higher mass densities, causing the photons to get more gravitationally red-shifted as they propagate towards Earth, an effect which is stronger than the initial higher temperature of the photons emitted from these regions.

[5] In fact, the by far strongest variation comes from the motion of the earth relative to the cosmic rest frame (the frame in which the CMB is the most isotropic). This Doppler shift is being subtracted from the measured CMB to obtain the distribution one would have seen if the earth was in the cosmic rest frame.

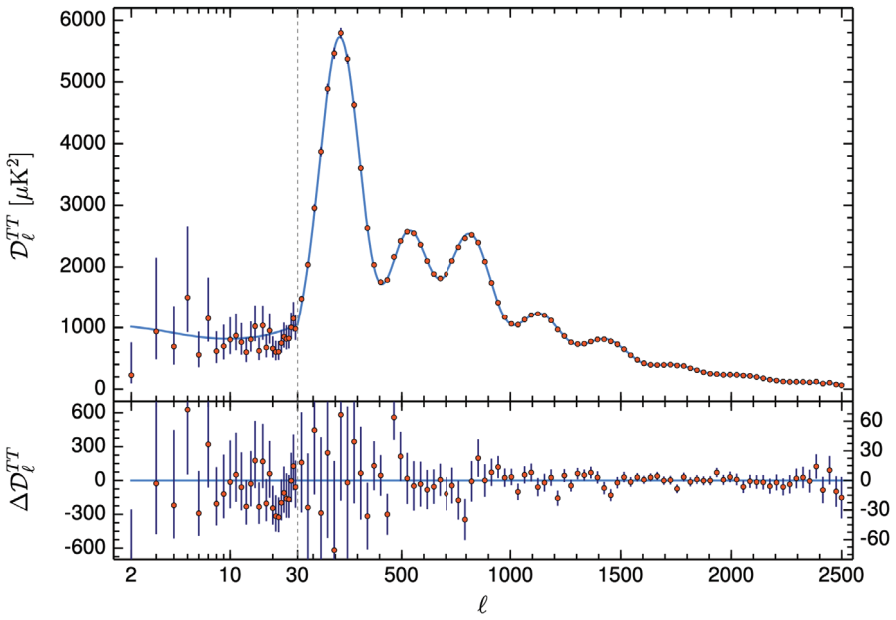

Figure 2.1: The CMB power spectrum taken from Planck 2018 [1]. The blue line is the theoretical prediction from ΛCDM with the best fit cosmological parameters given in eq. (2.11), and the red dots are the values inferred from the measurements of the CMB with 1σ error bars. The upper panel shows the spectrum, whereas the lower panel shows the discrepancy between the theoretical prediction and the measured result. Note that the horizontal scale changes from logaritmic to linear at the vertical dashed line at $\ell = 30$, and that also the vertical plot range in the lower panel is reduced by a factor of 10 to the right of the line.

coefficients $\mathcal{D}_\ell^{TT}$ shown in fig. 2.1 and defined as [3]

$$\begin{aligned} \mathcal{D}_\ell^{TT} &= \sum_m \frac{\ell(\ell+1)}{2\pi} \left\langle a_{\ell m}^{T*} a_{\ell m}^{T} \right\rangle , \\ a_{\ell m}^{T} &= \int \mathrm{d}\,\hat{\mathbf{n}}\, Y_{\ell m}^{*}\left(\hat{\mathbf{n}}\right) \delta T\left(\hat{\mathbf{n}}\right) , \end{aligned} \tag{2.10}$$

with $\delta T\left(\hat{\mathbf{n}}\right)$ being the temperature perturbation of the CMB photons coming from direction $\hat{\mathbf{n}}$, and $Y_{\ell m}$ are spherical harmonics. $\langle\rangle$ refers to the average over the temperature perturbations simulated with different initial conditions for the density distribution of the universe. These are typically assumed to be Gaussian distributed, and the expected distribution of $\delta T\left(\hat{\mathbf{n}}\right)$ is simulated from the Einstein equations and hydrodynamical equations.

$\delta T(\hat{\mathbf{n}})$ is also inferred from measurements of the photon temperature of the CMB, and the averaging $\langle\rangle$ is done over different patches of the sky. For small ℓ there are few sky patches to average over, causing the error bars in fig. 2.1 to be large in this region of ℓ. Comparing the measurements to the simulations one infer the values of the parameters in the ΛCDM that cause the simulations to fit the measurements.

The effect of DM is intuitively understood, as DM can clump together much more efficiently than baryons. This is due to DM not feeling the radiation pressure of the photons. It then forms gravitational wells around which the baryons oscillate in what is called baryon acoustic oscillations. In particular, the absence of DM would suppress the second peak in fig. 2.1. As such, DM is vital in forming the CMB, and from fig. 2.1 one sees that there is excellent agreement between the prediction of the ΛCDM shown in the blue line and the measurement shown with the red dots.

These best fit values of Ω_r, Ω_m, Ω_k, Ω_Λ, Ω_b and Ω_{DM} producing the blue line in fig. 2.1 are not only fit to the CMB but also to other measurements. They are [1]

$$\begin{aligned} \Omega_m &= 0.3111\,, \quad \Omega_b = 0.0492\,, \quad \Omega_{\text{DM}} = 0.2630\,, \\ \Omega_r &= 0.0001\,, \quad \Omega_k = 0.0007\,, \quad \Omega_\Lambda = 0.6889\,, \end{aligned} \tag{2.11}$$

from which one sees that DM makes up 26.3% of the energy content and 84.5% of the matter content of the universe. Note that $\Omega_m \gg \Omega_k$ and $\Omega_\Lambda \gg \Omega_k$, so there is no time (no value of $z > 0$) at which the term proportional to Ω_k dominates the right hand side of eq. (2.8). In fact, the measured value of Ω_k is compatible with 0 and usually neglected. The curvature being negligible is typically explained with inflation, in which the early universe goes through an accelerating expansion, flattening out any initial curvature.

2.2 Structure formation

ΛCDM does not only explain the CMB; it also describes how the clumping of DM that give rise to the CMB goes on to form structures such as galaxy clusters, galaxies and dwarf galaxies. This is done with hydrodynamical simulations, such as the code Evolution and Assembly of GaLaxies and their Environment (EAGLE) [75]. In these hydrodynamical simulations, one sim-

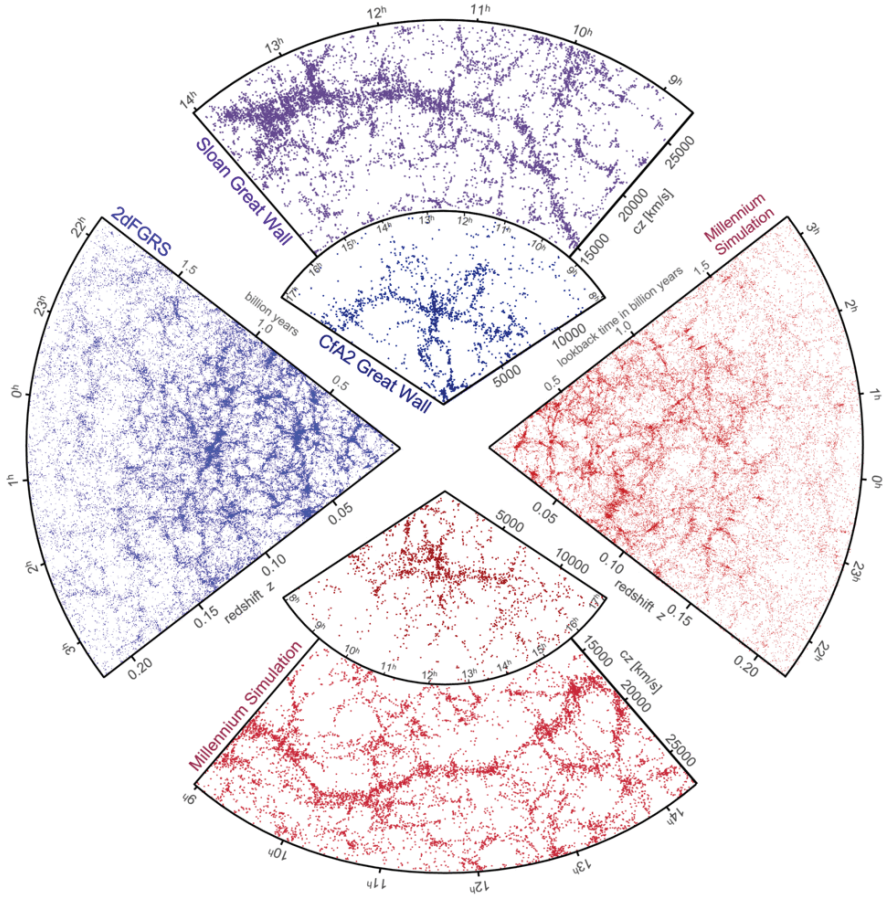

Figure 2.2: A comparison between observed galaxy distribution (blue) and simulated galaxy distribution (red) taken from [74].

ulates baryon gas and DM particles with masses of order $10^6 M_\odot$ to $10^7 M_\odot$ in a box of between $(50\text{Mpc})^3$ and $(100\text{Mpc})^3$. $M_\odot$ denotes the mass of the Sun. As the particle mass is much greater than the stellar mass, such simulations cannot treat phenomena such as star formation, Active Galactic Nucleus (AGN) and supernova. These phenomena are important for the evolution of galaxies as the radiation from these cause the galaxy to loose mass, and interacts with the gas in the InterStellar Medium (ISM) influencing the ISM distribution in and around the galaxy. The impact of these phenomena referred to as subgrid physics is accounted for using a range of tools discussed in section 4 of ref. [75].

With simulations such as EAGLE one obtains a distribution of matter in

the universe in the form of galaxy clusters and galaxies. This distribution of galaxies can be compared to observations of galaxy distributions in our universe [76] to find excellent statistical agreement [77]. This agreement is examplified in fig. 2.2 where the observed galaxy distribution is shown in blue and the simulated galaxy distribution is shown in red.

Simulations such as EAGLE can also be used to obtain detailed information about the distribution of DM in our galaxy. In doing so one picks out galaxies from the simulation which have a distribution of visible matter similar to what is observed in the Milky Way. One can then take the velocities of the simulated DM particles in the Milky Way like galaxies to span the possible distributions of the true DM velocities in the Milky Way. Below, more direct observations of the DM distribution in galaxies is discussed.

2.3 Astrophysical observations

As discussed above DM is crucial in the theoretical description of how galaxies and galaxy clusters form and evolve. The presence of DM in galaxies can also be measured more directly. In this section two such methods for measuring the DM density in galaxies and galaxy clusters will be covered, namely weak gravitational lensing and galactic rotation curves.

Weak Gravitational Lensing

General relativity [81] describes how massive objects bend the trajectory of light, a phenomenon known as gravitational lensing. Large astrophysical objects such as galaxy clusters create a measurable lensing effect when light passes through it, which in turn can be used to infer the gravitational mass of the astrophysical object. One generally distinguishes between strong and weak lensing. By strong lensing one refers to gravitational lensing strong enough to produce multiple images around a massive object. This is due to the photons being "caught" and orbiting multiple times around the massive object before escaping. Weak lensing, on the other hand, causes small distortions of the original image, and from these distortions one can statistically infer the mass density that caused the distortions.

This is done for the Bullet Cluster in fig. 2.3, an iconic image often used to visualize the presence of the DM in our universe. The image shows two galaxy

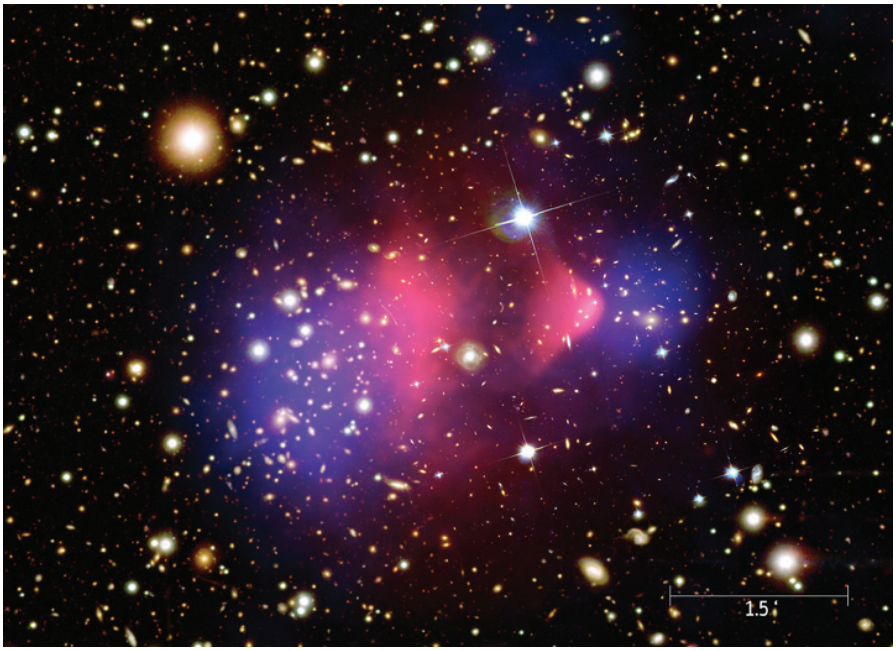

Figure 2.3: Image of the Bullet Cluster showing gravitational lensing in blue [78], x-ray radiation in red [79] together with the optical image [80].

clusters that are colliding. The blue color shows the mass density inferred from gravitational lensing whereas the red color shows the x-ray density. As the x-rays mostly come from the hydrogen gas that makes up most of the visible mass of the galaxy, the red color shows the density of visible mass whereas the blue color shows the density of total mass. As is evident from the image, the hydrogen clouds collide with each other and lose some of their velocity, whereas the clouds of dark matter pass through each other largely unaffected. This is a strong indicator of the presence of a large invisible mass that interacts weakly enough with itself and with the visible matter that it does not cause observable friction.

Galactic Rotation Curves

The discrepancy between the gravitational mass and the visible mass was first observed in the 1930s by Zwicky and Smith. They compared the velocity of galaxies with the velocities they would expect from the visible mass in the Coma and Virgo clusters respectively [83], [84]. They found a discrepancy

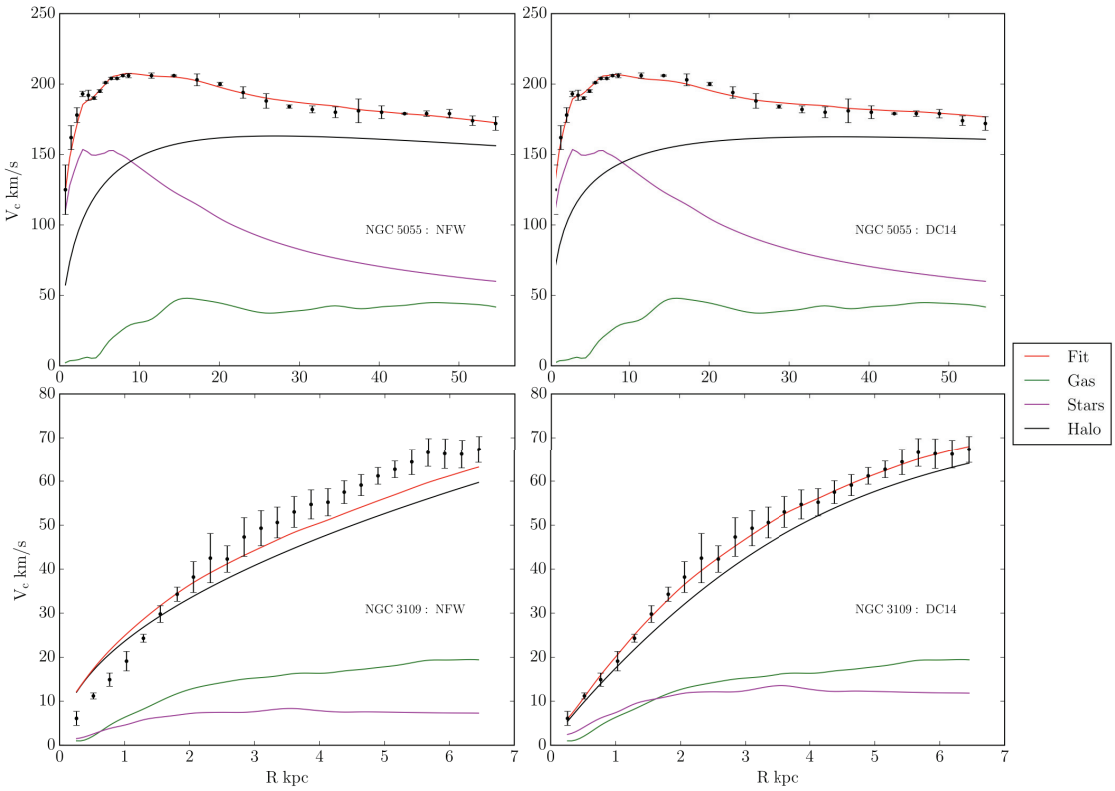

Figure 2.4: Plot from ref. [82] showing measured velocity distribution of visible objects in galaxies as function of distance from the galactic center. The pink and green lines show the contribution to the velocity distribution from the stars and gas clouds in the galaxy, respectively, whereas the black line shows the best fit DM distribution obtained with the NFW method in the panels to the left and the DC14 method in the panels to the right. Together these contributions produce the red line. The upper two panels are for a galaxy with a large mass, whereas the lower panels are for a galaxy with a smaller mass.

which Zwicky referred to as dark matter[6]. The circular velocity v of a gravitationaly bound object is given from Newtonian physics [85] as[7]

$$v(r) = \sqrt{4\pi r \int_0^r \mathrm{d}\tilde{r}\, \rho(\tilde{r})}\,, \tag{2.12}$$

[6]Zwicky was however not the first who used the term dark matter to refer to invisible matter in the universe. See [4] for details on the history of dark matter.

[7]For simplicity ρ is here taken to be spherically symmetric, an approximation which is not as bad as it might seem as most of the mass of galaxies is believed to lie in an approximately spherically symmetric dark matter halo rather than in the stellar disk.

so the distribution of the mass density of the galaxy, $\rho(r)$, can be inferred by measuring $v(r)$ for multiple r. These measurements of $v(r)$ are shown in fig. 2.4. There the expected velocity distributions from the mass density of the observed gas, the observed stars and best fit DM halo is shown with the green, pink, and black line respectively. Combined they form the red line as the predicted total velocity. In the top two panels we see the galactic rotation curve for a large galaxy in which the DM density dominates outside a radius of 10 kpc from the galactic center, whereas for smaller galaxies such as what is shown in the lower panels the DM dominates everywhere.

CHAPTER 3

Particle Dark Matter

In chapter 2 we saw that measurements of the CMB together with other astrophysical observations show that DM makes up 84.5% of the matter content of the universe. These measurements do, however, not give information of the underlying structure of DM[1]. There have been suggested several models to account for this invisible mass, ranging from massive objects such as primordial black holes to elementary particles or composites thereof. In this thesis DM is assumed to be particles described by Quantum Field Theory (QFT). From a Direct Detection (DD) perspective one can divide DM models into two classes; DM particles that scatters elastically with SM particles depositing parts of its kinetic energy to the SM particles; and DM particles that can be absorbed by SM particles, depositing its entire mass-energy. These two classes of DM models will be discussed briefly below, before mechanisms by which it can be created will be discussed.

[1] It should be noted that the similarity between the abundance of DM and SM particles suggest that they might have a common origin and therefore have some form of interaction. This common origin would also indicate that the DM and SM particles should have similar masses, i.e. that the DM particle should have a mass in the meV to TeV range, much of which is probeable with direct detection experiments discussed in chapter 4.

3.1 A Selection of DM Models

WIMPs and sub-GeV DM

WIMPs are stable Weakly Interacting Massive Particles interacting with the standard model through the weak force. WIMPs are highly motivated from the WIMP miracle mentioned in the introduction, and particles with the properties of WIMPs naturally arise in extensions to the SM such as Supersymmetry [86]–[88]. In order for the observed abundance of DM to be produced via the freeze-out mechanism to be discussed later in this chapter they need to have a mass larger than about 2 GeV [40]. They serve as the benchmark model for most DD experiments. With the lack of detection of such particles however, several models of lighter sub-GeV DM have also been proposed. These would be too light to induce detectable nuclear recoils. What these models have in common is that they feature a stable DM particle which couples to the SM via a mediator lighter than the gague bosons mediating the weak force. The lighter mediator relaxes the lower bound on the WIMP mass of 2 GeV for production via freeze out. These particles can scatter elastically with SM particles, transferring (a fraction of) its kinetic energy to the SM particle. As such, from a DD perspective these models can be characterized by the mass of the DM particle and the nature of its interaction with the SM. The most popular (and simplest) is the dark photon model.

Dark Photon Model

The dark photon model extends the standard model with an additional $U(1)$ gauge group with which the dark photon A'_μ is the associated gauge boson. The DM particle χ couples to the dark photon in the same way as the photon couples to charged particles in the SM. Furthermore this dark photon is usually taken to kinetically mix with the SM photon, giving rise to interactions between DM and ordinary charged matter. In this model, the dark sector is described by the Lagrangian

$$\mathscr{L}_D = \bar{\chi}(i\gamma^\mu D_\mu - m_\chi)\chi + \frac{1}{4}F'_{\mu\nu}F'^{\mu\nu} + m^2_{A'}A'_\mu A'^\mu + \varepsilon F_{\mu\nu}F'^{\mu\nu}\,, \qquad (3.1)$$

with the covariant derivative defined as

$$D_\mu \chi = \partial_\mu \chi - i g_D A'_\mu \chi \,, \tag{3.2}$$

where g_D is the gauge coupling corresponding to the dark $U(1)$ gauge group, $F'^{\mu\nu}$ is the dark photon field strength tensor, $m_{A'}$ is the dark photon mass and ϵ is the kinetic mixing strength. This model has the advantage that the dark photon behaves like the SM one, which is well understood and leads to a simple expression for the DM-SM scattering cross section. The above Lagrangian is for a spin 1/2 DM particle, but DM particles with other spins are also extensively studied in the literature.

Other Non-Standard Interactions

Using the dark photon model as a benchmark might however cause one to miss potential signatures of DM caused by other more complicated interactions. Covering all possible interactions DM can have with SM requires Effective Field Theory (EFT) approaches, discussed in section 4.3. It can however be illustrative considering a few non-standard interactions DM can have with SM to show how their signatures differ from that of the dark photon model. In Papers 1, 2 and 4 non-standard interactions are considered to illustrate potential deviations from the phenomenology of the dark photon model [72], [89]. Dark matter could interact with the photon field through an electric dipole moment,

$$\mathscr{L}_{\text{int}} = \frac{g}{\Lambda}\, i\bar{\chi}\sigma^{\mu\nu}\gamma^5\chi\, F_{\mu\nu} \,, \tag{3.3a}$$

where g is the coupling strength and Λ is the energy scale at which the electric dipole is generated. Likewise, the DM particle can have a non-zero magnetic dipole moment described by the Lagrangian interaction term

$$\mathscr{L}_{\text{int}} = \frac{g}{\Lambda}\, \bar{\chi}\sigma^{\mu\nu}\chi\, F_{\mu\nu} \,, \tag{3.3b}$$

where again g and Λ are the coupling and the energy scale at which the magnetic dipole is generated, respectively. Dark matter might also interact

through the anapole interaction,

$$\mathscr{L}_{\text{int}} = \frac{g}{2\Lambda^2}\,\bar{\chi}\gamma^{\mu}\gamma^{5}\chi\,\partial^{\nu}F_{\mu\nu}\,. \tag{3.3c}$$

In Papers 1, 3, 4, 5 and 7 EFT is used to calculate the rate at which DM with these interactions scatters off bound electrons leaving observable signatures in direct detection experiments. In Paper 2 we go beyond the above mentioned non-standard interactions and look at generic DM-electron interactions for spin 0, spin 1/2 and spin 1 DM.

Axion (Like Particle)

Axions and Axion Like Particles (ALPs) is a class of models for DM consisting of bosons with a mass of a few eV and below. The axion was originally proposed as a solution to the CP problem of QCD, in which QCD generically break CP symmetry via the Lagrangian term

$$\mathscr{L}_{\theta} = \overline{\theta}\frac{\alpha_s}{8\pi}G^{\mu\nu a}\tilde{G}^{a}_{\mu\nu}\,, \tag{3.4a}$$

with $G^{\mu\nu a}$ being the gluon field strength tensor and its dual being $\tilde{G}^{\mu\nu a} \equiv \epsilon^{\mu\nu\rho\sigma}G^{a}_{\rho\sigma}/2$. This term in the Lagrangian would generate an electric dipole moment for the neutron, the lack of observation of which requires $\overline{\theta} \lesssim 10^{-10}$ [90]. This required smallness of $\overline{\theta}$ is remarkable as $\overline{\theta}$ receives contributions from two independent quantities that happen to cancel almost exactly [91]; one contribution related to the strong force and one to the weak force. Known as the strong CP problem, the cancellation is popularly explained by the Peccei-Quinn mechanism [11], [12] in which the QCD axion field [13], [14], a, couples to the gluons via the Lagrangian term

$$\mathscr{L}_{\theta,a} = \left(\frac{a}{f_a} - \overline{\theta}\right)\frac{\alpha_s}{8\pi}G^{\mu\nu a}\tilde{G}^{a}_{\mu\nu}\,, \tag{3.4b}$$

with f_a being the axion decay constant. The ground state of the axion field corresponds to $a/f_a = \overline{\theta}$, eliminating the CP violating term [92]. The axion mass can be calculated with chiral perturbation theory to be [93]

$$m_a = \frac{f_\pi m_\pi}{f_a}\frac{\sqrt{m_u m_d}}{m_u + m_d} \approx \frac{10^{12}\,\text{GeV}}{f_a}\,5.691\,\mu\text{eV}\,, \tag{3.5}$$

with m_u, m_d and m_π being the masses of the up quark, down quark and pion respectively, and f_π being the pion decay width. The QCD axion mass is usually assumed to lie in the range $1\,\mu$eV to $100\,\mu$eV, as this is compatible with the axion being produced in an abundance matching what is observed of DM.

Since the above described QCD axion was proposed, several other particles with similar characteristics referred to colloquially as ALPs have been proposed. These do not solve the strong CP problem and take m_a and f_a to be free parameters independent of each other. This allows f_a to be tuned such that the observed abundance of DM is produced, a condition which can be satisfied for $10^{-20}\,\text{eV} \lesssim m_a \lesssim \text{eV}$. Both axions and ALPs can oscillate into photons giving observable astrophysical signatures, or be absorbed in detectors on earth depositing their entire mass-energy to SM particle(s). For a review of axions and ALPs, see i.e. ref. [91], [94].

3.2 On The Origin of Dark Matter

There are several ways in which the DM particles can be created in the abundance matching the observed one. The abundance can for instance be set by an asymmetry between the particle and anti-particle abundance [95] similar to the SM particles. DM can also be created from interactions with visible matter, through two mechanisms we discuss below; freeze out and freeze in.

Freeze Out

If the DM particles interact strongly enough with the SM particles to be in equilibrium with the thermal bath of SM, the abundance of DM is that for which the rate of annihilation matches that of creation[2]. As the universe expands, the density of both the SM particles and the DM particles is reduced, and so is the rate of annihilation and creation of DM particles. Furthermore, as discussed in the last section, the radiation in the thermal bath is red-shifted as the universe expands, causing the temperature to decrease.

As the temperature drops below the mass of the DM particles the creation rate becomes exponentially suppressed. For DM to remain in equilibrium with

[2] Annihilation requires DM particles and anti-particles to collide, and this becomes more frequent the more DM particles and anti-particles there are. As such, the density of DM particles will naturally tend towards the equilibrium.

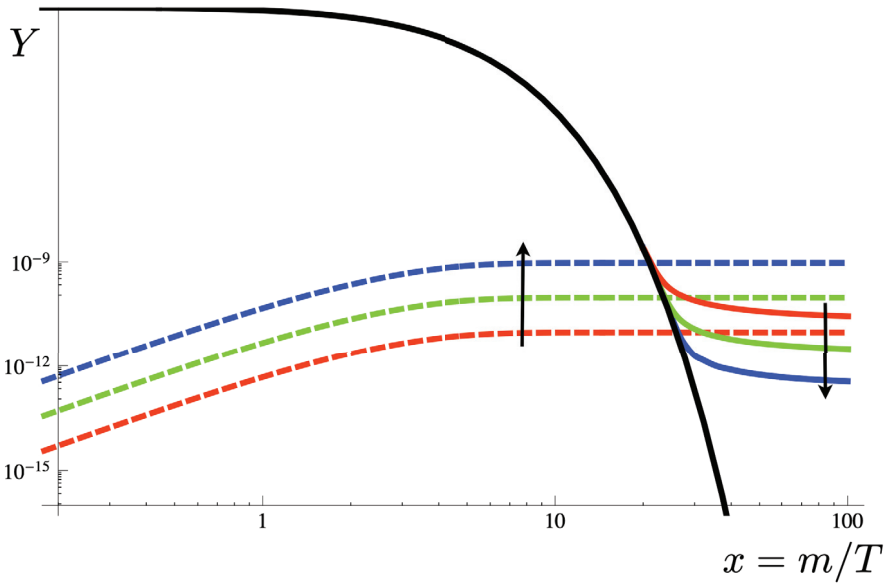

Figure 3.1: Illustrative plot of the freeze out mechanism (solid lines) and freeze in mechanism (dashed lines) from [96]. Y is the yield, and is proportional to the number of DM particles, whereas m here refers to the mass of the DM particle and T refers to the temperature of the SM bath. The black line shows the number of DM particles for DM in equilibrium, whereas the blue, green and red lines show the number of DM particles for different annihilation cross sections, with blue being the largest and red the smallest. The solid lines are for large enough annihilation cross sections that DM at high temperatures is in equilibrium with SM, whereas the dashed lines are for much smaller annihilation cross sections (but with the same relation between the colors) where DM never enters equilibrium with SM.

the SM particles the annihilation rate must also be exponentially suppressed, which in turn demands that the number of DM particles is exponentially suppressed. This suppression can be seen in fig. 3.1 for $m_\chi/T = x > 1$, where m_χ is the mass of the DM particle and T is the temperature of the SM bath.

As both the rate of creation and annihilation drops, however, DM departs from equilibrium; it freezes out. It can be shown that DM particles on average interact less than once between the time at which the interaction rate equals the Hubble rate and today. The DM particles are therefore taken to be decoupled when this condition is met.[3] After DM is decoupled the number of DM particles remains fixed until today. The number of DM particles today is

[3]It should be noted that even though DM has left chemical equilibrium it can still scatter elastically with the SM bath and thereby maintain kinetic equilibrium.

therefore determined by how much the number of DM particles is thermally suppressed before it leaves equilibrium (freezes out) [97], i.e. how long they stay in equilibrium. The stronger DM interacts with the SM particles, the longer it stays in equilibrium and the fewer DM particles survives until today. This effect can be seen from the solid lines in fig. 3.1 where the red solid line departs from equilibrium (the black line) before the blue solid line, giving a higher value of Y, which is proportional to the number of DM particles in the universe.

Freeze In

An alternative to the freeze out mechanism is freeze in. In this scenario the creation and annihilation cross sections are never large enough for DM to be in equilibrium with the SM bath; the annihilation of DM into SM particles is negligible at all times, whereas DM is created from the SM bath until the rate of creation becomes thermally suppressed by the temperature dropping below the mass of the DM particle. This evolution of the number of DM particles is shown by the dashed lines in fig. 3.1, where the red line corresponds to a lower creation cross section and thus a lower number of DM particles than the green and blue lines.

It is worth stressing that the creation cross sections of the dashed colored lines are much smaller than the ones for the solid colored lines, and as such the two mechanisms for production of DM complement each other by covering different ranges of creation cross sections. As a final word on DM creation it should be noted that the freeze in mechanism assumes that the initial number of DM particles is 0 (or at least very small). This means that whatever created the bath of SM particles cannot also have created a similarly large bath of DM particles. This assumption is not present in the freeze out regime, as a large initial DM bath would quickly annihilate into SM particles bringing the DM bath and the SM bath into equilibrium.

CHAPTER 4

Direct Detection of Dark Matter

As mentioned in the introduction, there are three main strategies for detection of DM. Collider searches involve accelerating SM particles to high energies and colliding them, causing the creation of additional particles. If DM is created, it will leave the detector undetected[1], carrying away momentum and energy. The detected particles will then seem to violate energy and momentum conservation, and from the missing energy-momentum one can conclude that undetectable particle(s) have been created. From the detected particles one can then reconstruct the interaction in which the DM was created[2].

Indirect detection experiments are searching for SM particles created by annihilating DM particles in space. If the DM particles have a mass similar to or larger than the massive particles in the SM, it can annihilate into high energy SM particles. These particles can be detected on Earth as cosmic

[1] There are also experiments attempting to detect high-velocity DM particles created from collisions of SM particles.

[2] This is similar to how the hints of the existence of the neutrino first emerged. It was noticed that electrons produced by beta decay took continuous energy values rather than the fixed energy of the nuclear transition. The existence of an electrically neutral (and thus at the time not detectable) particle with which the electron share the energy from the nuclear transition was proposed and later detected.

rays, gamma rays and neutrinos. As there also are other galactic sources of cosmic rays, the challenge is to distinguish cosmic rays due to DM from rays produced by other sources. Indirect detection can also be used to search for signals coming from models of lighter dark matter particles. Examples of this is impacts of axions on stellar physics and galactic gamma ray propagation, and radio flashes produced by axion condensates colliding with neutron stars.

Dark matter direct detection experiments are low background experiments searching for rare scattering events of DM with detector materials, where the DM deposits energy and momentum to the detector material. This deposited energy and momentum is then detected by means that vary between the experiments. In this chapter direct detection will be discussed. In the first section the Standard Halo Model (SHM) describing the density and velocity distribution of the DM near Earth will be covered, before the attention is moved to nuclear recoils in the second section. In the third section EFT is discussed before it in the fourth section is applied to DM electron scattering. The framework presented there is developed in the papers attached to this thesis.

4.1 The Standard Halo Model

In section 2.2 it was discussed how DM velocity distributions can be obtained from hydrodynamical simulations such as EAGLE. These simulations are computationally expensive, so the density and velocity distribution of DM is typically described by the SHM. The velocity distribution of DM particles in the SHM is obtained by assuming that the DM particles are Boltzmann-distributed in the galactic rest frame with the circular orbit velocity $v_0 = 238\,\mathrm{km/s}$ [98] being the most likely speed. Furthermore, the population of DM particles with velocities larger than the escape velocity of the galaxy $v_{\mathrm{esc}} = 544\,\mathrm{km/s}$ [98] is neglected, as these are assumed to largely have left the galaxy. This gives

$$f_{\mathrm{galaxy}}(\mathbf{v}) = \frac{1}{N} \exp\left[-\frac{\mathbf{v}^2}{v_0^2}\right] \Theta\left(v_{\mathrm{esc}} - |\mathbf{v}|\right) , \tag{4.1}$$

which is the DM velocity distribution in the galactic rest frame, with N being a normalisation factor. The Earth moves relative to the galactic rest frame with a velocity $\mathbf{v}_e$. At the time Paper 1 was published there was no consensus

on the value of v_e and we used $v_e = 244\text{km/s}$. Afterwards $v_e = 250.5\,\text{km/s}$ [98] got established as the standard in the DM community, and we use this value for Papers 2-6.

The motion of the Earth through the galaxy means that the velocity distribution of the DM particles reaching Earth is shifted to become

$$f_\chi(\mathbf{v}) = \frac{1}{N_{\text{esc}}\pi^{3/2}v_0^3}\exp\left[-\frac{(\mathbf{v}+\mathbf{v}_e)^2}{v_0^2}\right]\Theta\left(v_{\text{esc}} - |\mathbf{v}+\mathbf{v}_e|\right)\,, \tag{4.2}$$

with

$$N_{\text{esc}} \equiv \text{erf}(v_{\text{esc}}/v_0) - 2(v_{\text{esc}}/v_0)\exp\left[-v_{\text{esc}}^2/v_0^2\right]/\sqrt{\pi}\,, \tag{4.3}$$

being a normalisation factor and erf being the error function. Note that the distribution in eq. (4.2) is skewed in the direction of $-\mathbf{v}_e$, which is usually referred to as the direction of the DM wind.

Another important property of DM is the local DM density ρ_χ, i.e. the density of DM in the vicinity of Earth. In this thesis $\rho_\chi = 0.4\,\text{GeV/cm}^3$ is used, a value compatible with the findings of ref. [99], where $\rho_\chi = 0.385 \pm 0.027\,\text{GeV/cm}^3$ and $\rho_\chi = 0.389 \pm 0.025\,\text{GeV/cm}^3$ was found, depending on the assumed overall DM density profile. Other authors in the DM community are using $\rho_\chi = 0.3\,\text{GeV/cm}^3$ to ensure conservative results.

4.2 Nuclear Recoils

If dark matter scatters elastically with a nucleus, it deposits momentum and energy to the nucleus, causing it to recoil. Most direct detection experiments are designed to detect such nuclear recoils. As the nucleus has a mass of several GeV, and the velocity of DM in the vicinity of Earth is of order 10^{-3} in natural units, a DM particle of similar mass to that of the nucleus can deposit energies in the keV range. Specifically, the nucleus has a negligible initial state kinetic energy in the lab frame, and recoils with an energy given as [100]

$$E' = \frac{\mu_{\chi N}^2 v^2}{m_N}\left(1 - \cos\theta_R\right)\,, \tag{4.4}$$

where $\mu_{\chi N}$ is the reduced mass of the DM-nucleus system, v is the velocity of the incoming DM particle, m_N is the mass of the nucleus and θ_R is the angle between the path of the recoiled nucleus and that of the incoming DM

particle. The rate of these nuclear recoils is then given as

$$\frac{\mathrm{d}\,R}{\mathrm{d}\,E'} = \frac{\rho_\chi}{m_\chi m_N} \int \mathrm{d}^3\, v\, v f_\chi(\mathbf{v}) \frac{\mathrm{d}\,\sigma_{\chi N}}{\mathrm{d}\,E'}\,, \tag{4.5}$$

where $\sigma_{\chi N}$ is the DM nucleus scattering cross section.

Spin (In)Dependent Interactions

One usually takes the cross section to consist of a spin dependent (SD) and a spin independent (SI) term,

$$\frac{\mathrm{d}\,\sigma_{\chi N}}{\mathrm{d}\,E'} = \frac{m_N}{2\mu_{\chi N}^2 v^2} \left[\sigma_{\chi N}^{SI} F_{SI}^2 + \sigma_{\chi N}^{SD} F_{SD}^2\right]\,, \tag{4.6}$$

where $\sigma_{\chi N}^{SI}$ and $\sigma_{\chi N}^{SD}$ are the spin independent and spin dependent interaction cross sections respectively. They are given as

$$\sigma_{\chi N}^{SI} = \frac{4\mu_{\chi N}^2}{\pi} \left[Z f_p + (A - Z) f_n\right]^2\,, \tag{4.7a}$$

$$\sigma_{\chi N}^{SD} = \frac{32 G_F \mu_{\chi N}^2}{\pi} \frac{J+1}{J} \left[a_p \langle S_p\rangle + a_n \langle S_n\rangle\right]^2\,, \tag{4.7b}$$

with f_p (a_p) and f_n (a_n) being the spin independent (dependent) coupling of DM to the protons and the neutrons, respectively. $\langle S_p\rangle$ and $\langle S_n\rangle$ are proton and neutron spin factors.

Finally, F_{SI} and F_{SD} are the nuclear form factors [101]. They are introduced to account for the complicating fact that nuclei are not elementary particles; They have an internal structure which, depending on the momentum transfer, can be probed in a scattering with DM. A popular approximation for F_{SI} is the Helm form factor [102], given as

$$F_{SI} \approx F_{\mathrm{Helm}} = \left(\frac{3 j_1\left(q R_1\right)}{q R_1}\right)^2 e^{-q^2 s^2/2}\,, \tag{4.8}$$

where j_1 is the spherical Bessel function, q is the transferred momentum from the DM particle to the recoiling nucleus, $s \approx 1\,\mathrm{fm}$ is the nuclear skin thickness and $R_1 \approx 1.25 A^{1/3}\,\mathrm{fm}$ is the effective nuclear radius. For a review of nuclear recoils, see [100].

$\mathcal{O}_1 = \mathbb{1}_{\chi e}$	$\mathcal{O}_{12} = \mathbf{S}_\chi \cdot \left(\mathbf{S}_e \times \mathbf{v}_{\rm el}^\perp\right)$
$\mathcal{O}_3 = i\mathbf{S}_e \cdot \left(\frac{\mathbf{q}}{m_e} \times \mathbf{v}_{\rm el}^\perp\right)$	$\mathcal{O}_{13} = i\left(\mathbf{S}_\chi \cdot \mathbf{v}_{\rm el}^\perp\right)\left(\mathbf{S}_e \cdot \frac{\mathbf{q}}{m_e}\right)$
$\mathcal{O}_4 = \mathbf{S}_\chi \cdot \mathbf{S}_e$	$\mathcal{O}_{14} = i\left(\mathbf{S}_\chi \cdot \frac{\mathbf{q}}{m_e}\right)\left(\mathbf{S}_e \cdot \mathbf{v}_{\rm el}^\perp\right)$
$\mathcal{O}_5 = i\mathbf{S}_\chi \cdot \left(\frac{\mathbf{q}}{m_e} \times \mathbf{v}_{\rm el}^\perp\right)$	$\mathcal{O}_{15} = i\mathcal{O}_{11}\left[\left(\mathbf{S}_e \times \mathbf{v}_{\rm el}^\perp\right) \cdot \frac{\mathbf{q}}{m_e}\right]$
$\mathcal{O}_6 = \left(\mathbf{S}_\chi \cdot \frac{\mathbf{q}}{m_e}\right)\left(\mathbf{S}_e \cdot \frac{\mathbf{q}}{m_e}\right)$	$\mathcal{O}_{17} = i\frac{\mathbf{q}}{m_e} \cdot \boldsymbol{\mathcal{S}} \cdot \mathbf{v}_{\rm el}^\perp$
$\mathcal{O}_7 = \mathbf{S}_e \cdot \mathbf{v}_{\rm el}^\perp$	$\mathcal{O}_{18} = i\frac{\mathbf{q}}{m_e} \cdot \boldsymbol{\mathcal{S}} \cdot \mathbf{S}_e$
$\mathcal{O}_8 = \mathbf{S}_\chi \cdot \mathbf{v}_{\rm el}^\perp$	$\mathcal{O}_{19} = \frac{\mathbf{q}}{m_e} \cdot \boldsymbol{\mathcal{S}} \cdot \frac{\mathbf{q}}{m_e}$
$\mathcal{O}_9 = i\mathbf{S}_\chi \cdot \left(\mathbf{S}_e \times \frac{\mathbf{q}}{m_e}\right)$	$\mathcal{O}_{20} = \left(\mathbf{S}_e \times \frac{\mathbf{q}}{m_e}\right) \cdot \boldsymbol{\mathcal{S}} \cdot \frac{\mathbf{q}}{m_e}$
$\mathcal{O}_{10} = i\mathbf{S}_e \cdot \frac{\mathbf{q}}{m_e}$	$\mathcal{O}_{21} = \mathbf{v}_{\rm el}^\perp \cdot \boldsymbol{\mathcal{S}} \cdot \mathbf{S}_e$
$\mathcal{O}_{11} = i\mathbf{S}_\chi \cdot \frac{\mathbf{q}}{m_e}$	$\mathcal{O}_{22} = i\left(\frac{\mathbf{q}}{m_e} \times \mathbf{v}_{\rm el}^\perp\right) \cdot \boldsymbol{\mathcal{S}} \cdot \mathbf{S}_e$

Table 4.1: Interaction operators spanning the non-relativistic effective theory of spin 0, 1/2 and 1 DM-electron interactions[70]–[72], [103]–[105]. $\mathbf{S}_e$ ($\mathbf{S}_\chi$) is the electron (spin 1/2 DM) spin, $\mathbf{v}_{\rm el}^\perp = \mathbf{v} - \boldsymbol{\ell}/m_e - \mathbf{q}/(2\mu_{\chi e})$, where $\mu_{\chi e}$ is the DM-electron reduced mass, $\mathbf{v}_{\rm el}^\perp$ is the transverse relative velocity and $\mathbb{1}_{\chi e}$ is the identity in the DM-electron spin space. Finally, $\boldsymbol{\mathcal{S}}$ is the vector DM polarization matrix, and arises in models of spin 1 DM.

4.3 Non-relativistic Effective Field Theory

A more general description of the interaction between DM and SM target particles than the SI/SD framework described above is that of Non-Relativistic Effective Field[3] Theory (NR-EFT). As the name suggests, NR-EFT is an effective theory that describes scatterings between non-relativistic particles. In the lab on Earth, the SM target particle is typically non-relativistic. DM bound to our galaxy is also non-relativistic, as can be seen from eq. (4.2), where $f_\chi = 0$ for $v > v_{\rm e} + v_{\rm esc} \approx 795\,{\rm km/s} = 0.0027c$.

An elastic scattering between a free DM and a free SM particle is in general characterized by the spins of the DM and SM particle, as well as 4 vectorial degrees of freedom; The initial and final state DM momentum and the initial

[3] The name effective field theory is misleading as the theory is expressed in terms of effective interaction operators rather than effective fields. The name is still being widely used, mostly because the abbreviation EFT is well established in the context of high energy physics, and these effective operator based theories will therefore be referred to as EFTs in this thesis.

and final state SM momentum. One of these vector degrees of freedom is eliminated by momentum conservation. Yet another is eliminated by using that for non-relativistic particles the scattering process must be Galilean invariant. The non-relativistic scattering is thus determined by two independent momenta together with the spins of the DM and SM particles. In the context of DM electron scattering a common choice of independent momenta are the dimensionless quantities $\mathbf{q}/m_e$ and $\mathbf{v}_{\rm el}^{\perp} = \mathbf{v} - \boldsymbol{\ell}/m_e - \mathbf{q}/(2\mu_{\chi e})$, where $\mathbf{q}$ is the momentum transferred from the DM particle with mass m_χ to the electron with mass m_e. $\mathbf{v}$ is the velocity of the initial state DM particle, and $\boldsymbol{\ell}$ is the momentum of the initial state electron. $\mu_{\chi e}$ is the reduced mass of the DM electron system. $\mathbf{v}_{\rm el}^{\perp}$ has the property that $\mathbf{v}_{\rm el}^{\perp} \cdot \mathbf{q} = 0$ for elastic scatterings.

The spin of the DM particle $\mathbf{S}_\chi$ and the spin of the electron $\mathbf{S}_e$ can then be combined with $\mathbf{q}/m_e$ and $\mathbf{v}_{\rm el}^{\perp}$ to form effective operators. The number of effective operators that can be formed is in principle infinite, but since both $v_{\rm el}^{\perp} \ll 1$ and $q/m_e \ll 1$ we restrict ourselves to consider operators at leading order in $\mathbf{v}_{\rm el}^{\perp}$ and second order[4] in $\mathbf{q}/m_e$. The resulting operators are shown in tab. 4.1 for DM spins ≤ 1. $\mathcal{O}_2 = \mathbf{v}_{\rm el}^{\perp} \cdot \mathbf{v}_{\rm el}^{\perp}$ and $\mathcal{O}_{16} = \left(\mathbf{S}_\chi \cdot \mathbf{v}_{\rm el}^{\perp}\right)\left(\mathbf{S}_e \cdot \mathbf{v}_{\rm el}^{\perp}\right)$ are not included in the table as they are of second order in $\mathbf{v}_{\rm el}^{\perp}$. The free particle scattering amplitude can be written in terms of the effective operators as,

$$\mathcal{M}(\mathbf{q}, \mathbf{v}_{\rm el}^{\perp}) = \sum_i c_i F_{{\rm DM},i}(q) \left\langle \mathcal{O}_i \right\rangle , \tag{4.9}$$

where c_i is a dimensionless coupling constant and $F_{DM,i}(q)$ absorbs any additional q-dependence. For example, products such as $\mathbf{q}/m_e \cdot \mathbf{q}/m_e = q^2/m_e^2\, \mathcal{O}_1$ are not treated as a separate operator, but rather as $\mathcal{O}_1$ with the q dependence absorbed in $F_{DM,1}(q)$.

The operators can be categorised based on whether they obey parity (P) and/or time reversal (T) symmetry. Both P and T reverse the 3-vectors, but

[4]For typical scatterings $v_{\rm el}^{\perp} \sim 10^{-3}$ whereas $q/m_e \sim Z_{\rm eff}\,\alpha \approx Z_{\rm eff}/137$ where $Z_{\rm eff}$ is of order a few. One therefore expands to first order in $v_{\rm el}^{\perp}$ and second order in q/m_e.

only T reverses the spin. From this one can see that

$$\begin{aligned}
&\mathcal{O}_1, \mathcal{O}_3, \mathcal{O}_4, \mathcal{O}_5, \mathcal{O}_6, \mathcal{O}_{17}, \mathcal{O}_{20} && \text{P-even and T-even,}\\
&\mathcal{O}_7, \mathcal{O}_8, \mathcal{O}_9, \mathcal{O}_{18} && \text{P-odd and T-even,}\\
&\mathcal{O}_{13}, \mathcal{O}_{14}, \mathcal{O}_{19}, \mathcal{O}_{22} && \text{P-even and T-odd,}\\
&\mathcal{O}_{10}, \mathcal{O}_{11}, \mathcal{O}_{12}, \mathcal{O}_{15}, \mathcal{O}_{21} && \text{P-odd and T-odd.}
\end{aligned} \tag{4.10}$$

The operators can also be categorised based on the powers they contain of q/m_e and $v_{\text{el}}^{\perp}$:

Operators	q/m_e and $v_{\text{el}}^{\perp}$ dependence
$\mathcal{O}_1$, $\mathcal{O}_4$	$\left(v_{\text{el}}^{\perp}\right)^0 \left(q/m_e\right)^0$
$\mathcal{O}_9$, $\mathcal{O}_{10}$, $\mathcal{O}_{11}$, $\mathcal{O}_{18}$	$\left(v_{\text{el}}^{\perp}\right)^0 \left(q/m_e\right)^1$
$\mathcal{O}_7$, $\mathcal{O}_8$, $\mathcal{O}_{12}$, $\mathcal{O}_{21}$	$\left(v_{\text{el}}^{\perp}\right)^1 \left(q/m_e\right)^0$
$\mathcal{O}_6$, $\mathcal{O}_{19}$, $\mathcal{O}_{20}$	$\left(v_{\text{el}}^{\perp}\right)^0 \left(q/m_e\right)^2$
$\mathcal{O}_3$, $\mathcal{O}_5$, $\mathcal{O}_{13}$, $\mathcal{O}_{14}$, $\mathcal{O}_{17}$, $\mathcal{O}_{22}$	$\left(v_{\text{el}}^{\perp}\right)^1 \left(q/m_e\right)^1$
$\mathcal{O}_{15}$	$\left(v_{\text{el}}^{\perp}\right)^1 \left(q/m_e\right)^2$.

(4.11)

For similar c_i and $F_{\text{DM},i}$, eq. (4.11) sorts the operators according to importance from top to bottom. Operators $\mathcal{O}_1$ and $\mathcal{O}_4$ dominate, which is why these operators are often taken as benchmark operators, and correspond to the SI and SD interactions discussed in section 4.2 respectively.

Following the mapping from the relativistic to the non-relativistic theory outlined in [103], the interactions in eqs. (3.1) and (3.3) are found to give rise

to the following non-zero c_i coefficients with corresponding $F_{DM,i}(q)$ [72]:

Dark Photon Interaction:

$$c_1 = \frac{4m_\chi m_e g_D \epsilon e}{q_{\text{ref}}^2 + m_{A'}^2} \qquad F_{\text{DM},1} = \frac{q_{\text{ref}}^2 + m_{A'}^2}{q^2 + m_{A'}^2} \tag{4.12a}$$

Electric Dipole Interaction:

$$c_{11} = \frac{16m_\chi m_e^2 g e}{q_{\text{ref}}^2 \Lambda} \qquad F_{\text{DM},11} = \frac{q_{\text{ref}}^2}{q^2} \tag{4.12b}$$

Magnetic Dipole Interaction:

$$c_1 = \frac{4m_e g e}{\Lambda} \qquad F_{\text{DM},1} = 1$$

$$c_4 = \frac{16m_\chi g e}{\Lambda} \qquad F_{\text{DM},4} = 1$$

$$c_5 = \frac{16m_\chi m_e^2 g e}{q_{\text{ref}}^2 \Lambda} \qquad F_{\text{DM},5} = \frac{q_{\text{ref}}^2}{q^2}$$

$$c_6 = -\frac{16m_\chi m_e^2 g e}{q_{\text{ref}}^2 \Lambda} \qquad F_{\text{DM},6} = \frac{q_{\text{ref}}^2}{q^2} \tag{4.12c}$$

Anapole Interaction:

$$c_8 = \frac{8m_\chi m_e g e}{\Lambda^2} \qquad F_{\text{DM},8} = 1$$

$$c_9 = -\frac{8m_\chi m_e g e}{\Lambda^2} \qquad F_{\text{DM},9} = 1 \tag{4.12d}$$

Note that the P and T parities of the interactions are contained in the effective operators making up the interactions. The magnetic dipole interaction being both P and T even is made up of only P and T even operators, whereas the anapole interaction being P odd and T even is made up of P odd and T even operators.

4.4 Electron Recoils from NR-EFT

Electron recoils can be generated from DM in two different ways; through the Migdal Effect [106], [107] by which a DM induced nuclear recoil is converted into an electron recoil; and through DM scattering directly off the electron, the latter of which will be discussed here. The rate at which DM scatters

electrons from an initial state 1 into a final state 2 is given as [72]

$$\mathscr{R}_{1\to 2} = \frac{n_\chi}{16 m_\chi^2 m_e^2} \int \frac{\mathrm{d}^3 q}{(2\pi)^3} \int \mathrm{d}^3 v f_\chi(\mathbf{v})(2\pi)\delta(E_f - E_i)\overline{|\mathcal{M}_{1\to 2}|^2}\,, \tag{4.13}$$

where $n_\chi = \rho_\chi/m_\chi$ is the local number density of DM particles, m_χ is the mass of the DM particle, $\mathbf{q}$ is the momentum transfered from the DM particle to the electron, and E_i and E_f is the initial and final energy of the DM-electron system, respectively. Finally, $\overline{|\mathcal{M}_{1\to 2}|^2}$ is the squared electron transition amplitude, given in terms of the initial state electron wave-function ψ_1, the final state electron wave-function ψ_2 and the free scattering amplitude $\mathcal{M}$ as [72]

$$\overline{|\mathcal{M}_{1\to 2}|^2} \equiv \overline{\left| \int \frac{\mathrm{d}^3 p_e}{(2\pi)^3}\, \psi_2^*(\mathbf{p}_e + \mathbf{q})\mathcal{M}(\mathbf{p}_e, \mathbf{p}_\chi, \mathbf{q})\psi_1(\mathbf{p}_e) \right|^2}\,, \tag{4.14}$$

where $\mathbf{p}_e$ and $\mathbf{p}_\chi$ is the initial state momentum of the electron and DM particle, respectively. $\mathcal{M}(\mathbf{p}_e, \mathbf{p}_\chi, \mathbf{q})$ is expanded in effective operators as in eq. (4.9).

Electrons bound in materials have a velocity of order $v = p_e/m_e \sim \alpha Z_{\text{eff}} \approx Z_{\text{eff}}/137$, with Z_{eff} being of order a few for electrons relevant to DD experiments. One can therefore Taylor expand the matrix element to first order in $\mathbf{p}_e/m_e$;

$$\mathcal{M} = \mathcal{M}|_{\mathbf{p}_e/m_e=0} + \frac{\mathbf{p}_e}{m_e} \cdot m_e \nabla_{\mathbf{p}_e} \mathcal{M}|_{\mathbf{p}_e/m_e=0}\,. \tag{4.15}$$

This expansion can now be inserted in eq. (4.14) to obtain

$$\begin{aligned}\overline{|\mathcal{M}_{1\to 2}|^2} =& \overline{\left|\mathcal{M}|_{\mathbf{p}_e/m_e=0}\right|^2} |f_{1\to 2}|^2 \\ &+ 2m_e \overline{\Re\left[\mathcal{M} f_{1\to 2} (\nabla_{\mathbf{p}_e}\mathcal{M}^*)|_{\mathbf{p}_e/m_e=0} \cdot (\mathbf{f}_{1\to 2})^*\right]} \\ &+ m_e^2 \overline{\left|(\nabla_{\mathbf{p}_e}\mathcal{M})|_{\mathbf{p}_e/m_e=0} \cdot \mathbf{f}_{1\to 2}\right|^2}\,,\end{aligned} \tag{4.16}$$

where the electron wave-function overlap integrals $f_{1\to 2}$ and $\mathbf{f}_{1\to 2}$ are given

as

$$f_{1\to 2} = \int \mathrm{d}^3x\, \psi_2^*(\mathbf{x}) e^{i\mathbf{x}\cdot\mathbf{q}} \psi_1(\mathbf{x})\,, \tag{4.17a}$$

$$\mathbf{f}_{1\to 2} = \int \mathrm{d}^3x\, \psi_2^*(\mathbf{x}) e^{i\mathbf{x}\cdot\mathbf{q}} \frac{i\nabla_{\mathbf{x}}}{m_e} \psi_1(\mathbf{x})\,. \tag{4.17b}$$

Below we will look at two special cases of eq. (4.17). First, we will consider electron excitation in crystals, in which ψ_1 and ψ_2 both correspond to electrons bound in a periodic system. This is following the work done in Paper 1 where we modelled DD signals in Silicon and Germanium. Then we will look at electron ejections in which case ψ_1 corresponds to a bound electron and ψ_2 to a free one. Electron ejections were used to model DD experiments in Papers 3, 4 and 5.

Electron Excitation in Periodic Systems

For processes in which DM causes the electron to be excited from an initial ground state to an excited state, both the initial and final state wave-function is on Bloch form [108], i.e.

$$\psi_{i\mathbf{k}}(\mathbf{x}) = \frac{1}{\sqrt{V}} \sum_{\mathbf{G}} u_i(\mathbf{k}+\mathbf{G}) e^{i(\mathbf{k}+\mathbf{G})\cdot\mathbf{x}}\,, \tag{4.18}$$

with i being the band index, $\mathbf{k}$ being the Brillouin zone momentum, $\mathbf{G}$ being the reciprocal lattice vector and V being the volume of the electron system. $u_i(\mathbf{k}+\mathbf{G})$ are the Bloch coefficients, normalized such that $\sum_{\mathbf{G}} |u_i(\mathbf{k}+\mathbf{G})|^2 = 1$ for all i and $\mathbf{k}$. As shown in Paper 1, inserting these wave-functions in eq. (4.17) gives

$$f_{i,\mathbf{k}\to i',\mathbf{k}'} = \sum_{\mathbf{G}\mathbf{G}'} \frac{u^*_{i',\mathbf{k}'} u_{i,\mathbf{k}}}{V} (2\pi)^3 \delta^3(\mathbf{k}+\mathbf{G}+\mathbf{q}-\mathbf{k}'-\mathbf{G}')\,, \tag{4.19a}$$

$$\mathbf{f}_{i,\mathbf{k}\to i',\mathbf{k}'} = -\sum_{\mathbf{G}\mathbf{G}'} \frac{u^*_{i',\mathbf{k}'} u_{i,\mathbf{k}}}{m_e V} (\mathbf{k}+\mathbf{G}) (2\pi)^3 \delta^3(\mathbf{k}+\mathbf{G}+\mathbf{q}-\mathbf{k}'-\mathbf{G}')\,, \tag{4.19b}$$

where the unprimed band indexes, brillouin zone momenta and reciprocal lattice vectors denote the initial state whereas the primed ones denote the

final state. Inserting eq. (4.19) into eq. (4.16) gives

$$\begin{aligned}\overline{\left|\mathcal{M}_{i,\mathbf{k}\to i',\mathbf{k}'}\right|^2} =& \sum_{\Delta\mathbf{G}} \frac{(2\pi)^3\delta^3(\mathbf{k}+\mathbf{q}-\mathbf{k}'-\Delta\mathbf{G})}{V}\Bigg\{\overline{|\mathcal{M}|^2}\left|f'_{i,\mathbf{k}\to i',\mathbf{k}'}\right|^2 \\ &+ 2m_e\overline{\Re\left[\mathcal{M}f'_{i,\mathbf{k}\to i',\mathbf{k}'}(\nabla_{\mathbf{p}_1}\mathcal{M}^*)_{\mathbf{p}_1=0}\cdot\left(\mathbf{f}'_{i,\mathbf{k}\to i',\mathbf{k}'}\right)^*\right]} \\ &+ m_e^2\overline{\left|(\nabla_{\mathbf{p}_1}\mathcal{M})_{\mathbf{p}_1=0}\cdot\mathbf{f}'_{i,\mathbf{k}\to i',\mathbf{k}'}\right|^2}\Bigg\} \\ \equiv& \sum_{\Delta\mathbf{G}} \frac{(2\pi)^3\delta^3(\mathbf{k}+\mathbf{q}-\mathbf{k}'-\Delta\mathbf{G})}{V}\times\overline{\left|\mathcal{M}'_{i,\mathbf{k}\to i',\mathbf{k}'}\right|^2}\,, \end{aligned} \tag{4.20}$$

with the primed electron wave-function overlap integrals being defined as

$$f'_{i,\mathbf{k}\to i',\mathbf{k}'} \equiv \sum_{\mathbf{G}} u^*_{i'}\left(\mathbf{k}'+\mathbf{G}+\Delta\mathbf{G}\right)u_i\left(\mathbf{k}+\mathbf{G}\right)\,, \tag{4.21a}$$

$$\mathbf{f}'_{i,\mathbf{k}\to i',\mathbf{k}'} \equiv -\frac{1}{m_e}\sum_{\mathbf{G}} u^*_{i'}\left(\mathbf{k}'+\mathbf{G}+\Delta\mathbf{G}\right)\left(\mathbf{k}+\mathbf{G}\right)u_i\left(\mathbf{k}+\mathbf{G}\right)\,. \tag{4.21b}$$

Eq. (4.13) gives the rate of scattering from an initial state $1\to\{i,\mathbf{k}\}$ to a final state $2\to\{i',\mathbf{k}'\}$. The total rate of excitations is obtained by summing over i and i', and integrating over $\mathbf{k}$ and $\mathbf{k}'$:

$$\mathscr{R} = 2\sum_{ii'}\int_{\mathrm{BZ}}\frac{V\mathrm{d}^3k}{(2\pi)^3}\int_{\mathrm{BZ}}\frac{V\mathrm{d}^3k'}{(2\pi)^3}\,\mathscr{R}_{i\mathbf{k}\to i'\mathbf{k}'}\,, \tag{4.22}$$

where the integrals are carried out over the Brillouin Zone of the crystal and the factor of 2 in front accounts for there being 2 electrons in every initial state band i. Inserting eqs. (4.13) and (4.20) into the above equation gives

$$\begin{aligned}\mathscr{R} =& \frac{\pi n_\chi V}{4m_\chi^2 m_e^2}\int\mathrm{d}^3q\int\mathrm{d}^3v\,f_\chi(\mathbf{v})\delta\left(E_{i'\mathbf{k}'}-E_{i\mathbf{k}}+\frac{q^2}{2m_\chi}-\mathbf{q}\cdot\mathbf{v}\right) \\ &\times\sum_{\Delta\mathbf{G}ii'}\int_{\mathrm{BZ}}\frac{\mathrm{d}^3k}{(2\pi)^3}\int_{\mathrm{BZ}}\frac{\mathrm{d}^3k'}{(2\pi)^3}\overline{\left|\mathcal{M}'_{i,\mathbf{k}\to i',\mathbf{k}'}\right|^2}\delta^3(\mathbf{k}+\mathbf{q}-\mathbf{k}'-\Delta\mathbf{G})\,. \end{aligned} \tag{4.23}$$

Rearranging and introducing an integral over ΔE together with $\delta(\Delta E - E_{i\mathbf{k}}+$

$B_1 = \left\lvert f'_{i,\mathbf{k}\to i',\mathbf{k}'} \right\rvert^2$	$B_5 = i\frac{\mathbf{q}}{m_e} \cdot \left[\mathbf{f}'_{i,\mathbf{k}\to i',\mathbf{k}'} \times \left(\mathbf{f}'_{i,\mathbf{k}\to i',\mathbf{k}'}\right)^*\right]$
$B_2 = \frac{\mathbf{q}}{m_e} \cdot (f'_{i,\mathbf{k}\to i',\mathbf{k}'})(\mathbf{f}'_{i,\mathbf{k}\to i',\mathbf{k}'})^*$	$\mathbf{B}_6 = f'_{i,\mathbf{k}\to i',\mathbf{k}'} \left(\mathbf{f}'_{i,\mathbf{k}\to i',\mathbf{k}'}\right)^*$
$B_3 = \left\lvert \mathbf{f}'_{i,\mathbf{k}\to i',\mathbf{k}'} \right\rvert^2$	$\mathbf{B}_7 = \frac{\mathbf{q}}{m_e} \times f'_{i,\mathbf{k}\to i',\mathbf{k}'} \left(\mathbf{f}'_{i,\mathbf{k}\to i',\mathbf{k}'}\right)^*$
$B_4 = \left\lvert \frac{\mathbf{q}}{m_e} \cdot \mathbf{f}'_{i,\mathbf{k}\to i',\mathbf{k}'} \right\rvert^2$	

Table 4.2: Products of electron wave-function overlap integrals generating the material response functions.

$E_{i'\mathbf{k}'}$), the total rate of DM electron scatterings can be written as

$$\begin{aligned}\mathscr{R} =& \frac{n_\chi N_{\text{cell}}}{64\pi m_\chi^2 m_e^2} \int \mathrm{d}^3 q \int \mathrm{d}\, \ln(\Delta E) \int \mathrm{d}^3 v\, f_\chi(\mathbf{v}) \delta\left(\Delta E + \frac{q^2}{2m_\chi} - \mathbf{q}\cdot\mathbf{v}\right) \\ & \times \sum_{l=1}^{r} \Re\left(R_l^*(q,v) W_l(\mathbf{q},\Delta E)\right) , \end{aligned} \tag{4.24}$$

where N_{cell} is the number of unit cells in the system, R_l is the dark matter response function, and the material physics is contained within W_l defined as

$$\begin{aligned} W_l(\mathbf{q},\Delta E) =& (4\pi)^2 V_{\text{cell}} \Delta E \sum_{\Delta\mathbf{G} i i'} \int_{\text{BZ}} \frac{\mathrm{d}^3 k}{(2\pi)^3} \int_{\text{BZ}} \frac{\mathrm{d}^3 k'}{(2\pi)^3} B_l \\ & \times \delta^3(\mathbf{q} - \mathbf{k}' - \Delta\mathbf{G} + \mathbf{k}) \delta(\Delta E - E_{i\mathbf{k}} + E_{i'\mathbf{k}'}) . \end{aligned} \tag{4.25}$$

B_l are functions built from the electron wave function overlap integrals in eq. (4.21), given in tab. 4.2.

The material response functions in eqs. (4.25) depend on sums over bands and reciprocal lattice vectors, and integrals over Brillouin zone momentum of Bloch coefficients u. In Paper 1, W is computed using Density Functional Theory (DFT), which is reviewed in the next chapter.

The rate in eq. (4.24) is the total rate of DM electron scatterings. In Si [48], [49], [51] and Ge [50], [51] based experiments the measureable quantity is rather number of events creating Q electron hole pairs. The number of electron hole pairs created in a given event depends on the deposited energy, ΔE as

$$Q(\Delta E) = 1 + \lfloor (\Delta E - E_{\text{gap}})/\epsilon \rfloor , \tag{4.26}$$

where the band gap energy E_{gap} and the energy required to create an additional electron hole pair ϵ depends on the material:

$$\begin{aligned} \epsilon &= 3.8\,\text{eV} && \text{Silicon} \\ \epsilon &= 3.0\,\text{eV} && \text{Germanium} \\ E_{\text{gap}} &= 1.2\,\text{eV} && \text{Silicon} \\ E_{\text{gap}} &= 0.67\,\text{eV} && \text{Germanium}\,. \end{aligned} \tag{4.27}$$

Electron Ejections

Let us now consider processes in which DM ejects the electron from the initial state system. As shown in Paper 3, describing the final state as a plane wave,

$$\psi_2(\mathbf{x}) \to \psi_{\mathbf{k}'} = \frac{1}{\sqrt{V}} e^{i\mathbf{k}'\cdot\mathbf{x}}\,, \tag{4.28}$$

greatly simplifies the electron overlap integrals in eq. (4.17):

$$f_{1\to\mathbf{k}'} = \frac{1}{\sqrt{V}} \tilde{\psi}_1(\mathbf{k}' - \mathbf{q})\,, \tag{4.29a}$$

$$\mathbf{f}_{1\to\mathbf{k}'} = \frac{\mathbf{q} - \mathbf{k}'}{m_e \sqrt{V}} \tilde{\psi}_1(\mathbf{k}' - \mathbf{q}) = \frac{(\mathbf{q} - \mathbf{k}')}{m_e} f_{1\to\mathbf{k}'}\,. \tag{4.29b}$$

The two overlap integrals are the same up to a factor of $(\mathbf{q} - \mathbf{k}')/m_e$. This means that all the combinations of overlap integrals listed in tab. 4.2 can be written in terms of a single overlap integral combination which is simply proportional to $\left|\tilde{\psi}_1(\mathbf{k}' - \mathbf{q})\right|^2$. This in turn allows us to write the matrix element in terms of a single free particle and material response function,

$$\mathcal{M}_{1\to\mathbf{k}'} = R_{\text{free}}(\mathbf{k}', \mathbf{q}, \mathbf{v})\; W(\mathbf{k}' - \mathbf{q}, E_e)\,, \tag{4.30}$$

and the rate of electron ejections is then given as

$$\begin{aligned} R = \frac{n_\chi N_{\text{cell}}}{32\pi^2 m_\chi^2 m_e^2} \int \mathrm{d}^3k' \int \mathrm{d}\,E_e \int \mathrm{d}^3q \int \mathrm{d}^3v\, f_\chi(\mathbf{v}) \\ \times\, \delta\left(\Delta E_e + \frac{q^2}{2m_\chi} - \mathbf{v}\cdot\mathbf{q}\right) R_{\text{free}}(\mathbf{k}', \mathbf{q}, \mathbf{v})\; W(\mathbf{k}' - \mathbf{q}, E_e)\,. \end{aligned} \tag{4.31}$$

Above $\mathbf{k}'$ is the final state momentum of the ejected electron and $E_e \leq 0$ is the energy of the initial state electron relative to the highest occupied state. $\Delta E_e = (k')^2 + \Phi - E_e$ is the energy deposited to the electron and Φ is the work function, i.e. the minimum energy required to move an electron from the bound state to a free state at rest. $R_{\text{free}}(\mathbf{k}', \mathbf{q}, \mathbf{v})$ is the free particle response function depending only on the physics of scattering of free particles.

$$W(\boldsymbol{\ell}, E_e) = \frac{V_{\text{cell}}}{(2\pi)^3} \sum_i \int_{\text{BZ}} \frac{\mathrm{d}^3 k}{(2\pi)^3} \delta\left(E_e - E_i(\mathbf{k})\right) \times \left|\widetilde{\psi}_{i\mathbf{k}}(\boldsymbol{\ell})\right|^2 , \tag{4.32}$$

is the material response function encoding all the material properties needed to calculate the ionisation rate. In the above described formalism the material is assumed to consist of N_{cell} equal parts with volume V_{cell} referred to as unit cells. The response function in eq. (4.32) is the response of a single unit cell.

If the initial state is on Bloch form,

$$\psi_{i\mathbf{k}}(\mathbf{x}) = \frac{1}{\sqrt{V}} \sum_{\mathbf{G}} u_i(\mathbf{k} + \mathbf{G}) e^{i(\mathbf{k}+\mathbf{G})\cdot\mathbf{x}} , \tag{4.33}$$

W becomes

$$\begin{aligned} W(\boldsymbol{\ell}, E_e) = V_{\text{cell}} \sum_i \int_{\text{BZ}} \frac{\mathrm{d}^3 k}{(2\pi)^3} \delta\left(E_e - E_i(\mathbf{k})\right) \\ \times \sum_{\mathbf{G}} |u_i(\mathbf{k} + \mathbf{G})|^2 \delta^{(3)}(\mathbf{k} + \mathbf{G} - \boldsymbol{\ell}) . \end{aligned} \tag{4.34}$$

So far in the discussion of electron ejections we have modelled the final state as a plane wave, i.e. a free electron that does not interact with any other charges. In practice, however, the electron will leave behind a positively charged system that alters the electron wave-function. In Papers 3 and 4 we argue that graphene and carbon nanotubes (CNTs) being an excellent conductor causes the positive charge to disperse quickly, reducing the impact it has on the final state electron wave-function. This is supported by very good agreement between experimentally measured and DFT-calculated graphene Compton profiles [109]. We therefore approximate the electron wave-function as being a plane wave when treating graphene and CNTs.

In Paper 5 we treat DM induced ejections from liquid Xenon, a material with poor electric conductivity. A popular approximation for the final state electron

wave-function is positive energy hydrogen solutions [72], [110], [111], in which the final state electron wave function is obtained by solving the Schrödinger equation in a Z_{eff}/r potential. Z_{eff} is the unscreened charge experienced by the final state electron, and depends on the orbital from which it is ejected.

A way in which the distortion of the final state wave-function can be taken into account is by introducing a Fermi factor. The square of the electron wave-function overlap integral in eq. (4.17a) can be rewritten in momentum space as

$$|f_{1\to 2}|^2 = \left| \int \frac{\mathrm{d}^3 k'}{(2\pi)^3} \tilde{\psi}_2^*(\mathbf{k}') \tilde{\psi}_1(\mathbf{k}' - \mathbf{q}) \right|^2 . \tag{4.35}$$

Assuming that $\tilde{\psi}_2(\mathbf{k}')$ is approximately a plane wave which peaks at $\mathbf{k}' = \mathbf{k}''$, the above integral can be approximated as

$$\begin{aligned} |f_{1\to 2}|^2 &= \left| \tilde{\psi}_1(\mathbf{k}'' - \mathbf{q}) \int \frac{\mathrm{d}^3 k'}{(2\pi)^3} \tilde{\psi}_2^*(\mathbf{k}') \right|^2 , \\ &= \left| \tilde{\psi}_1(\mathbf{k}'' - \mathbf{q}) \psi_2^*(0) \right|^2 , \\ &\approx \left| \tilde{\psi}_1(\mathbf{k}'' - \mathbf{q}) \right|^2 |\psi_2(0)|^2 , \end{aligned} \tag{4.36}$$

For ψ_2 being obtained by solving the Schrödinger equation in a Z_{eff}/r potential,

$$|\psi_2(0)|^2 = \frac{2\pi Z_{\text{eff}}(E_e)}{a_0 k' \left(1 - e^{-\frac{2\pi Z_{\text{eff}}(E_e)}{a_0 k'}}\right)} \equiv F(k', E_e) , \tag{4.37}$$

where $a_0 = 1/(\alpha m_e)$ is the Bohr radius and $F(k', E_e)$ is the Fermi factor, and can be multiplied with the wave-function in eq. (4.32) to account for the distortion of the final state wave-function.

CHAPTER 5

Density Functional Theory

For several applications ranging from biology, medicine and chemistry to material science, computer chips and dark matter direct detection experiments, understanding the electronic structure in liquids and solids is crucial. The electronic structure is described by the many-body Schrödinger equation, and solving it for various systems is therefore a central problem in (low energy) physics. The relevant system to describe a solid is that of $n_e \sim 10^{24}$ electrons all interacting with each other and with an almost as large number of nuclei. Accounting for all these particles and all the interactions between them is computationally impossible. Density Functional Theory (DFT) overcomes this by introducing an electron density experiencing an effective potential. In this chapter a brief overview of DFT will be given.

5.1 Hohenberg, Kohn, Sham and Exchange-Correlation Energies

A wave-function describing N particles in 3 dimensions is in general $3N$ dimensional. The curse of dimensionality makes it unfeasible to compute the

N-particle wave-function even fairly small N such as $N = 8$ for the electrons in an oxygen atom[1]. The Hohenberg-Kohn theorems [112] mend this, by showing that for a fixed number of particles in a fixed potential, the total energy of the system can be expressed in terms of the particle density, and is minimised for the ground state. This greatly simplifies the problem, as the density is 3 dimensional independently of the number of particles in the system.

Kohn developed this further together with Sham, producing a set of central equations in DFT known as the Kohn-Sham equations proposed in ref. [113],

$$E = -\frac{1}{2}\sum_i \int \mathrm{d}^3\, x\, \psi_i^*(\mathbf{x})\nabla^2\psi_i(\mathbf{x}) + \frac{1}{2}\int \mathrm{d}^3\, x\, \mathrm{d}^3\, x'\, \frac{n_e(\mathbf{x})n_e(\mathbf{x}')}{|\mathbf{x}-\mathbf{x}'|} + \int \mathrm{d}^3\, x \left[V_{\mathrm{ext}}(\mathbf{x}) + \epsilon_{xc}\left(n_e^{\uparrow}(\mathbf{x}), n_e^{\downarrow}(\mathbf{x})\right)\right] n_e(\mathbf{x})\,, \tag{5.1a}$$

$$\epsilon_i\psi_i(\mathbf{x}) = \left\{-\frac{1}{2}\nabla^2 + V_{\mathrm{ext}}(\mathbf{x}) + \int \mathrm{d}^3\, x'\, \frac{n_e\left(\mathbf{x}'\right)}{|\mathbf{x}-\mathbf{x}'|} + \frac{\mathrm{d}}{\mathrm{d}n_e}\left(n_e\epsilon_{xc}(n_e)\right)\right\}\psi_i(\mathbf{x})\,, \tag{5.1b}$$

$$n_e(\mathbf{x}) = \sum_i |\psi_i(\mathbf{x})|^2\,, \tag{5.1c}$$

where E is the energy of the electron system, which can be minimized to obtain the ground state. $n_e(\mathbf{x}) = n_e^{\uparrow}(\mathbf{x}) + n_e^{\downarrow}(\mathbf{x})$ is the electron number density of the system with $n_e^{\uparrow}(\mathbf{x})$ and $n_e^{\downarrow}(\mathbf{x})$ being the density of spin up and spin down electrons respectively. ψ_i are orthogonal Kohn-Sham orbitals with energy ϵ_i, and $V_{\mathrm{ext}}(\mathbf{x})$ is the external potential experienced by the electrons. The Kohn-Sham orbitals are taken to be approximations of the electron wave-functions[2] and can be calculated from eq. (5.1b), which is similar to the 1 particle Schrödinger equation. Finally, ϵ_{xc} is known as the exchange and correlation energy per electron, taking quantum effects into account and making the 3 last terms in eq. (5.1b) an effective potential. As a first approximation in ref. [113], Kohn and Sham took $\epsilon_{xc}\left(n_e^{\uparrow}(\mathbf{x}), n_e^{\downarrow}(\mathbf{x})\right)$ to be that of a free electron gas of density n_e. This approximation for ϵ_{xc} is known as the Local Spin

[1] Sampling 10 points per dimension in an oxygen atom requires 10^{24} points.

[2] Within the condensed matter community it is being debated how good approximations these Kohn-Sham orbitals are to the "true" electron wave-functions. The ground state Kohn-Sham orbitals are a more robust outcome of the calculation than the excited states, and is therefore less controversial. The Kohn-Sham orbitals do however reproduce several observables such as the dielectric constant, and are typically the best available description of the electron wave-functions in solids.

Density (LSD) approximation.

Another more accurate approximation for the exchange and correlation energy is that of Generalized Gradient Approximation (GGA) [114], in which the exchange and correlation energy is allowed to also depend on the gradient of the electron density, that is

$$\epsilon_{xc} = \epsilon_{xc}^{GGA}\left(n_e^{\uparrow}(\mathbf{x}), n_e^{\downarrow}(\mathbf{x}), \nabla n_e^{\uparrow}(\mathbf{x}), \nabla n_e^{\downarrow}(\mathbf{x})\right) . \tag{5.2}$$

GGA does in general perform better than LSD, and is the standard choice for DFT calculations today. In Papers 1, 3 and 5 we use pseudopotentials obtained with GGA.

5.2 Plane Wave Self-Consistent DFT Calculation

When obtaining the material response functions in eq. (4.25) and (4.34) , the ground state electron wave-functions have to be found. This can be done using a self-consistent DFT calculation. One then iteratively solves the Kohn-Sham equations (5.1) to find a converged $n_e(\mathbf{x})$ that minimizes the energy E in eq. (5.1a). The Kohn-Sham orbitals are expanded in terms of plane waves[3] using the Bloch Theorem [108],

$$\psi_{i,\mathbf{k}}(\mathbf{x}) = \frac{1}{\sqrt{V}} \sum_{\mathbf{G}} u_i(\mathbf{k}+\mathbf{G})\, e^{i(\mathbf{k}+\mathbf{G})\cdot\mathbf{x}} , \tag{5.3}$$

where the number of plane waves included is set by the cut-off energy E_{cut}, by the relation

$$\frac{(\mathbf{k}+\mathbf{G})^2}{2m_e} \leq E_{\text{cut}} . \tag{5.4}$$

[3]Plane waves is only one of several possible basis in which to expand the wave-function. Other options include atomic orbitals.

The Bloch coefficients $u_i(\mathbf{k}+\mathbf{G})$ are found by iteratively going through the self consistency loop [115]:

$$\epsilon_i^{(n)}\psi_i^{(n)}(\mathbf{x}) = \left\{-\frac{1}{2}\nabla^2 + V_{\text{in}}^{(n)}(\mathbf{x})\right\}\psi_i^{(n)}(\mathbf{x})\,, \tag{5.5a}$$

$$n_e^{(n)}(\mathbf{x}) = \sum_i \left|\psi_i^{(n)}(\mathbf{x})\right|^2\,, \tag{5.5b}$$

$$V_{\text{out}}^{(n)}(\mathbf{x}) = V_{\text{ext}}(\mathbf{x}) + \int \mathrm{d}^3\,x'\,\frac{n_e^{(n)}(\mathbf{x}')}{|\mathbf{x}-\mathbf{x}'|} + \frac{\mathrm{d}}{\mathrm{d}n_e^{(n)}}\left(n_e^{(n)}\epsilon_{xc}(n_e^{(n)})\right)\,, \tag{5.5c}$$

where one could take $V_{\text{in}}^{(n+1)} = V_{\text{out}}^{(n)}$, although it has proven more efficient to take $V_{\text{in}}^{(n+1)} = (1-\beta)V_{\text{in}}^{(n)} + \beta V_{\text{out}}^{(n)}$ with β being a parameter valued between 0 and 1. V_{ext} is provided by an external Pseudo Potential, which allows for the electron orbitals closest to the nucleus[4] to be included in the external potential. One then does not need to obtain the Kohn-Sham orbitals for these core electrons. The iteration loop in eq. (5.5) is being carried out by `Quantum ESPRESSO` [116]–[118], which recasts eq. (5.5a) into a linear algebra eigenvalue problem and solves it, obtaining the Bloch coefficients, $u_i(\mathbf{k}+\mathbf{G})$. These can in turn be used to compute the material response functions in eq. (4.25), which is done in the `QEdark-EFT` code [119], described below.

5.3 `QEdark-EFT`

`QEdark-EFT` builds on `QEdark` [65], and exists in 3 slightly different versions, customised for Papers 1, 3 and 5. The version made for Paper 1 computes W_l from eq. (4.25) for all l. This is done by discretication, which converts the delta functions in the definition of W_l into Heaviside functions, and the integrals over Brillouin zone momentum into sums over discrete points. The Heaviside functions serve as bins in energy and momentum, and `QEdark-EFT` loops over the discreticed Brillouin zone momentum, bands and reciprocal lattice vectors. For each combination of these $u_i(\mathbf{k}+\mathbf{G})$ is loaded from a self-consistent DFT calculation performed with `Quantum ESPRESSO` and used to compute B_l. The contribution to W_l is then added to the bin identified from the band energy, Brillouin zone momentum and reciprocal lattice vector. The

[4] Often referred to as core electrons or core states

code then outputs W_l for a grid of momentum and energy. The versions for Paper 3 and 5 work similarly, but computes and outputs only a single W as defined in eq. (4.34). The version for Paper 3 outputs $W(\boldsymbol{\ell}, E_e)$, whereas the version in Paper 5 utilises the spherical symmetry of liquid Xenon to average over the directions of $\boldsymbol{\ell}$ and outputs $W(\ell, E_e)$. This lower dimensionality of W in Paper 5 makes the computation of the rate considerably faster than the computation in Paper 3.

The W-grid which is being output from `QEdark-EFT` is then loaded by a separate code which performs the integrals in eq. (4.24) for Paper 1 or the ones in eq. (4.31) for Paper 3 and 5. For Paper 1 we simply brute force computed the Riemann sum to obtain the rates of electron-hole pair creation, whereas for Papers 3 and 5 we used Monte Carlo methods.

CHAPTER 6

Neural Networks

Neural Networks (NNs) and Artificial Intelligence (AI) is an extremely powerful tool capable of disrupting a wide range of societal and scientific areas. As examples from biology it can be used for good such as solving the computationally expensive problem of protein folding [120] and bad such as designing more potent chemical weapons [121]. With the rapid increase in capabilities and generality of large language models such as GPT [122], LaMDA [123] and Mistral [124], superhuman artificial general intelligence seems likely in the coming decades.

NNs can also be used to speed up the calculation of DM induced signals in semiconductors, which is the focus of Paper 6. In the last two chapters we developed a formalism with which we can compute detector signals from DM electron scatterings. In the event of an observation of such a signal it will be necessary to perform parameter scans in order to match the signal to a set of EFT parameters. Since the EFT has several coupling coefficients the parameter scan will be performed in a many dimensional parameter space. Speeding up the evaluation of the DM induced signal is therefore needed. In Paper 6 we use a simple FeedForward Neural Network (FFNN) to quickly produce a large number of possible DM signals in Semiconductors needed to

carry out parameters scans.

6.1 Feedforward Neural Network

A FFNN is the simplest form of NN, in which the neurons do not form cycles, but rather where information only runs in one direction. An example of such a network is illustrated in fig. 6.1. We will in this section use this network as an example network when describing how it works and is trained. In practice the networks are considerably larger. The network in the figure has two hidden layers marked in yellow, an input layer in red which takes two scalars as input, $N_{1,1}$ and $N_{1,2}$ and an output layer which gives a single scalar as output, $N_{4,1}$. For a given $N_{1,1}$ and $N_{1,2}$ the network calculates

$$\begin{aligned} N_{2,i} &= f(b_{2,i} + \sum_{j=1}^{2} N_{1,j}\, \omega^1_{j,i})\,, \\ N_{3,i} &= f(b_{3,i} + \sum_{j=1}^{3} N_{2,j}\, \omega^2_{j,i})\,, \\ N_{4,1} &= f(\sum_{j=1}^{3} N_{3,j}\, \omega^3_{j,1})\,, \end{aligned} \tag{6.1}$$

or with vector notation

$$\mathbf{N}_k = f(\mathbf{b}_k + \mathbf{N}_{k-1}\omega^{k-1})\,, \tag{6.2}$$

where $\omega^k_{j,i}$ are called weights and $b_{k,i}$ are called biases. These are trainable parameters adjusted during training. f is the activation function, and a common choices are tanh, $\sigma(x) = 1/(1+e^{-x})$ and $\mathrm{ReLu}(x) = \max(x, 0)$

NNs are mostly trained using a technique called backpropagation. The NN is trained on a training set; a set of $N_{1,1}, N_{1,2}$ and corresponding true values of $N^T_{4,1}$. The network starts out with randomly initialised weights and biases. For $N_{1,1}, N_{1,2}$ the network then follows eq. (6.1) and computes its guess $N^G_{4,1}(\omega^3, b_3, \omega^2, b_2, \omega^1)$, which is a function of the randomly initiallized weights and biases. The difference between $N^T_{4,1}$ and $N^G_{4,1}$ is computed and referred to as the loss. A common choice for a loss function is mean square error, $E_{\mathrm{MSE}}(\omega^3, b_3, \omega^2, b_2, \omega^1) = \left(N^T_{4,1} - N^G_{4,1}(\omega^3, b_3, \omega^2, b_2, \omega^1)\right)^2$. One can

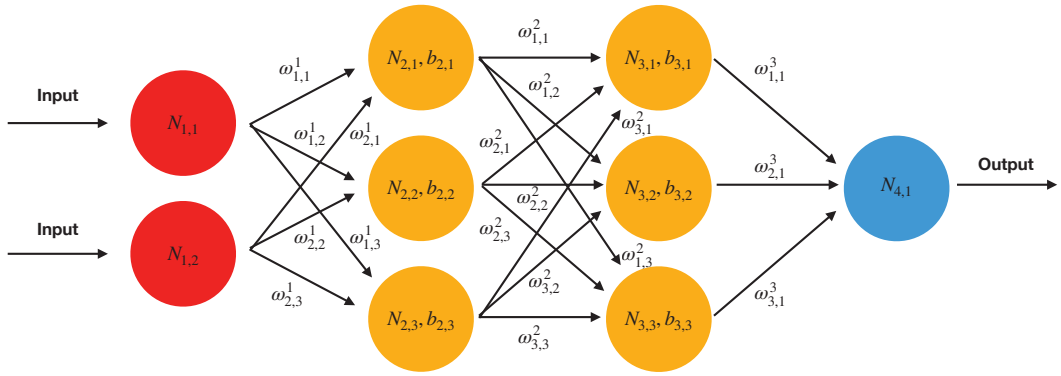

Figure 6.1: Illustration of a neural network with two hidden layers

then perform gradient decent on this error starting at the back,

$$
\begin{aligned}
\bar{\omega}^3_{j,1} &= \omega^3_{j,1} - r\frac{\partial}{\partial \omega^3_{j,1}} E_{\mathrm{MSE}}(\omega^3, b_3, \omega^2, b_2, \omega^1)\,, \\
\bar{b}_{3,i} &= b_{3,i} - r\frac{\partial}{\partial b_{3,i}} E_{\mathrm{MSE}}(\bar{\omega}^3, b_3, \omega^2, b_2, \omega^1)\,, \\
\bar{\omega}^2_{j,i} &= \omega^2_{j,i} - r\frac{\partial}{\partial \omega^2_{j,i}} E_{\mathrm{MSE}}(\bar{\omega}^3, \bar{b}_3, \omega^2, b_2, \omega^1)\,, \\
\bar{b}_{2,i} &= b_{2,i} - r\frac{\partial}{\partial b_{2,i}} E_{\mathrm{MSE}}(\bar{\omega}^3, \bar{b}_3, \bar{\omega}^2, b_2, \omega^1)\,, \\
\bar{\omega}^1_{j,i} &= \omega^1_{j,i} - r\frac{\partial}{\partial \omega^1_{j,i}} E_{\mathrm{MSE}}(\bar{\omega}^3, \bar{b}_3, \bar{\omega}^2, \bar{b}_2, \omega^1)\,,
\end{aligned}
\tag{6.3}
$$

where r is a tunable parameter called the training rate and barred quantities denote the updated values. The loop in eq. (6.3) is iterated several times during training. In practice one does not compute eq. (6.3) for the whole data set, but rather for a randomly selected subset with a method called stochastic gradient decent. One also does not compute E_{MSE} for a single $N^T_{4,1}$, but rather for a randomly selected subset of the training set, where then E_{MSE} is the mean squared error of the subset.

6.2 Computing DM Signals in Si and Ge With NN

In paper 1 we developed a framework to calculate the rate of DM events creating Q electron hole pairs in a crystal of Si or Ge. With this framework we can calculate the rate R_i of DM induced electron hole pairs Q_i as a function of the parameters characterising the DM model; m_χ, c_i and $F_{\mathrm{DM},i}(q)$. We restrict ourselves to treat long and short range interactions, i.e. $F_{\mathrm{DM},i}(q) = q_{\mathrm{ref}}^2/q^2$ and $F_{\mathrm{DM},i}(q) = 1$ and spin 1/2 DM. This means that there are 14 operators and two interaction ranges, giving a total of 28 operator and range combinations, each specified by a scalar referred to as a coupling. These 28 scalars together with the DM mass m_χ will serve as an input to a NN. The output will be the rates of events R_i creating Q_i electron hole pairs, where i runs from 1 to n.

The training set we generate by first drawing a random number of non-zero couplings m between 1 and 28 from a uniform distribution. We then draw m random numbers uniformly between -1 and 1, and assign them to random couplings, leaving the remaining couplings as 0. Different operators are suppressed by different powers of $v_{\mathrm{el}}^\perp$ and q/m_e as shown in eq. (4.11). For scatterings in crystals $q/m_e \sim \alpha = 1/137$ and $v_{\mathrm{el}}^\perp \sim 10^{-3}$, and couplings are rescaled by the inverse of the q/m_e and $v_{\mathrm{el}}^\perp$ dependence listed in eq. (4.11). The set of couplings are paired with a DM mass m_χ drawn from a logarithmic distribution and recast to lie between 0 and 1. Using the framework from paper 1 we then calculate R_i.

A challenge when having the NN predict R_i is that the rate varies over several orders of magnitude depending on the input parameters. Furthermore, R_i tends to co-variate for different i. We therefore have the NN output $n+1$ rather than n scalars, namely

$$s = \frac{\sum_i^n \ln(R_i)}{n}\,, \tag{6.4a}$$

$$R_i' = \ln(R_i) - s\,. \tag{6.4b}$$

This way the NN can learn the shape of the DM signal by learning to predict R_i' and learn the magnitude of the signal by predicting s. Even if it sometimes gets s and thus the magnitude of the signal wrong, it might still get R_i' and thus the shape of the signal right. Note that the parameters in eq. (6.4) blows up if $R_i = 0$ for any i. To avoid this the minimum m_χ is set such that R_i is

non-zero for all i, i.e.

$$m_\chi^{\min} > 2\frac{E_{\text{gap}} + \epsilon(n-1)}{(v_e + v_{\text{esc}})^2}\,. \tag{6.5}$$

For $n = 4$ and with the values from eq. (4.27) and $v_{\text{esc}} = 544\,\text{km/s}$ and $v_e = 250.5\text{km/s}$ from section 4.1.

$$\begin{aligned} m_\chi^{\min} &= 4\,\text{MeV} && \text{Silicon} \\ m_\chi^{\min} &= 3\,\text{MeV} && \text{Germanium}\,. \end{aligned} \tag{6.6}$$

In paper 6 we use TensorFlow [125] to train a FFNN to predict s and R_i' for $n = 4$ electron hole pairs. The network consists of an input layer with 29 neurons, 6 dense layers with 64, 128, 128, 64, 32, 16 neurons respectively, and finally an output layer with 5 neurons. We use the mean square error (MSE) as the loss function, and use ReLu as the activation function. To evaluate the performance of the network we look at the average relative error,

$$E = \left(\sum_i^N \sum_j^n \frac{\max(R_{j,i}^T/R_{j,i}^G,\, R_{j,i}^G/R_{j,i}^T)}{nN} \right) - 1\,. \tag{6.7}$$

We achieve a value of E of less than 3% when training on $N = 4.2 \times 10^6$ combinations of couplings and DM mass.

CHAPTER 7

Summary and Outlook

The nature of DM is one of the greatest unanswered questions in modern particle physics, and answering it requires both experimental and theoretical efforts. With the emergence of DD experiments sensitive to DM-electron scatterings, a theoretical understanding of these scatterings is crucial. The works of this thesis pushes the frontier of this theoretical understanding in two directions: By using NR-EFT to extend the range of DM models that can be considered by the experiments, and by using DFT to improve the modelling of the electronic structure in the detector materials.

In Paper 1, we model DM induced electronic excitations in crystals for general fermionic DM electron interactions. We find that depending on the nature of the DM-electron interaction, as many as 7 different crystal responses can be induced. 6 of these ways in which crystals can respond to an outer probe were theorised for the first time in Paper 1. We also present expected rates of DM induced electron-hole pair production for various models of DM, and use existing experimental data to constrain the parameters of the models.

In Paper 2, we expand the work to also include bosonic DM with spin 1. While spin 1 DM does not produce crystal responses different to the ones produced by spin 0 and 1/2 DM, the work demonstrates how these novel

crystal responses generically appear in a wide range of DM models. This is done by considering a wide range of simplified models, and showing that the novel responses from Paper 1 arise in many of them. It thus demonstrates the importance of taking all crystal responses into account when interpreting results of silicon and germanium based experiments.

In Paper 3, we mend discrepancies in the existing tight binding approximation in the literature, and argue that the tight binding approximation is poorly suited to obtain the electron density in graphene and CNTs. We also employ DFT, which we argue gives a better description of the electron density than the tight binding approximation in graphene. Having obtained the electron density, we use it to model DM induced electron ejections from graphene and CNTs. We show that when the final state wave-function is approximated as a plane wave, there is only one single material response function, proportional to the electron density. This work improves the state of the art modelling of graphene and CNTs for DM electron interaction, both from the material and from the DM side.

In Paper 4, we use the description of graphene and CNTs from Paper 3 to calculate the sensitivities of various experimental setups. Graphene and CNTs are both anisotropic materials, and therefore the rate of DM induced electron ejections depends on the direction the DM particle came from. We consider both graphene and CNTs, and both fixed and moving experimental setups. In the fixed setups, we consider CNTs or graphene detectors fixed in the lab. The goal of these experiments are to establish a daily modulation in the rate of electron ejections they observe. In the moving experimental setups, we consider two identical detectors facing in different directions, and tracking the DM wind. These experiments would attempt to establish a significant difference between the number of electron ejections observed in the two detectors. We compare the detector setups, and find large differences in the expected performance of the considered experimental setups. We do this comparison for several different forms of DM-electron interactions, and find that how the different setups perform is interaction type dependent.

In Paper 5, we use DFT to improve the modelling of liquid Xenon. Improving the description of liquid Xenon has a large impact, as the largest DD experiments currently use liquid Xenon as a detector material. Crucially we find that the liquid phase shifts and broadens the 5p electrons, leading to a dramatic increase in the expected number of DM induced events producing

single or few ionised electrons. This suggests that there is more to be gained than previously believed from lowering the detector threshold.

Finally, in Paper 6, we train a NN to take effective coupling constants and DM masses as inputs, and output rates of electron hole pair creation in Silicon and Germanium crystals. This work massively speeds up the evaluation of DM induced signals in these materials, and allows for performing parameter scans in a high-dimensional parameter space. This will become important in the event of an anomalous signal, and it demonstrates that NNs can be used to massively speed up such calculations.

Together, these works push the frontier of the theoretical understanding of DM-electron scattering in detector materials. Three very natural extensions to the works in this thesis are:

- Use DFT to model an array of CNTs. In Paper 3, we model a single CNT, and neglect the effects of the curvature of the CNT. In practice, CNTs used in experiments will be in the form of a CNT "forrest", where the different tubes interact with each other. Running a DFT calculation which includes the interactions between neighbouring CNTs would provide a more accurate description of the CNT based detector.

- Study daily modulation in graphene and CNTs taking high energy subpopulations of DM into account. In paper 4, we focus on the daily modulation pattern produced by the motion of the Earth through the DM halo of the Milky Way. This work could be extended by including DM particles not gravitationally bound to the Milky Way, such as DM particles coming from the Sun, cosmic ray upscattered DM particles, and DM particles coming from astrophysical structures such as the Large Magellanic Cloud.

- Model liquid Argon. In Paper 5, we model liquid Xenon. The other liquid noble gas widely used as a detector material is Argon. The Argon based experiments have somewhat worse sensitivity than the Xenon based ones, which is why we choose to focus on Xenon in paper 5. When modelling liquid Argon, much of the pipeline for Xenon can be reused. Furthermore, having a DFT model of liquid Argon would allow for a better comparison of the two detector materials.

References

[1] N. Aghanim *et al.*, "Planck 2018 results. VI. Cosmological parameters," *Astron. Astrophys.*, vol. 641, A6, 2020, [Erratum: Astron.Astrophys. 652, C4 (2021)].

[2] D. N. Spergel *et al.*, "First year Wilkinson Microwave Anisotropy Probe (WMAP) observations: Determination of cosmological parameters," *Astrophys. J. Suppl.*, vol. 148, pp. 175–194, 2003.

[3] N. Aghanim *et al.*, "Planck 2018 results. I. Overview and the cosmological legacy of Planck," *Astron. Astrophys.*, vol. 641, A1, 2020.

[4] G. Bertone and D. Hooper, "History of dark matter," *Rev. Mod. Phys.*, vol. 90, no. 4, p. 045 002, 2018.

[5] B. J. Carr, "The Primordial black hole mass spectrum," *Astrophys. J.*, vol. 201, pp. 1–19, 1975.

[6] S. W. Hawking, "Black hole explosions," *Nature*, vol. 248, pp. 30–31, 1974.

[7] Hawking, S. W., "Particle Creation by Black Holes," *Commun. Math. Phys.*, vol. 43, G. W. Gibbons and S. W. Hawking, Eds., pp. 199–220, 1975, [Erratum: Commun.Math.Phys. 46, 206 (1976)].

[8] B. Carr, F. Kuhnel, and M. Sandstad, "Primordial Black Holes as Dark Matter," *Phys. Rev. D*, vol. 94, no. 8, p. 083 504, 2016.

[9] B. P. Abbott *et al.*, "Observation of Gravitational Waves from a Binary Black Hole Merger," *Phys. Rev. Lett.*, vol. 116, no. 6, p. 061 102, 2016.

[10] J. D. Bekenstein, "Relativistic gravitation theory for the modified Newtonian dynamics paradigm," *Phys. Rev. D*, vol. 70, p. 083 509, 8 Oct. 2004.

[11] R. D. Peccei and H. R. Quinn, "Constraints Imposed by CP Conservation in the Presence of Instantons," *Phys. Rev. D*, vol. 16, pp. 1791–1797, 1977.

[12] Peccei, R. D. and Quinn, Helen R., "CP Conservation in the Presence of Instantons," *Phys. Rev. Lett.*, vol. 38, pp. 1440–1443, 1977.

[13] F. Wilczek, "Problem of Strong P and T Invariance in the Presence of Instantons," *Phys. Rev. Lett.*, vol. 40, pp. 279–282, 1978.

[14] S. Weinberg, "A New Light Boson?" *Phys. Rev. Lett.*, vol. 40, pp. 223–226, 1978.

[15] S. Dodelson and L. M. Widrow, "Sterile-neutrinos as dark matter," *Phys. Rev. Lett.*, vol. 72, pp. 17–20, 1994.

[16] Y. Fukuda *et al.*, "Evidence for oscillation of atmospheric neutrinos," *Phys. Rev. Lett.*, vol. 81, pp. 1562–1567, 1998.

[17] M. Apollonio *et al.*, "Limits on neutrino oscillations from the CHOOZ experiment," *Phys. Lett. B*, vol. 466, pp. 415–430, 1999.

[18] J. Schechter and J. W. F. Valle, "Neutrino Masses in SU(2) x U(1) Theories," *Phys. Rev. D*, vol. 22, p. 2227, 1980.

[19] B. Moore, "Evidence against dissipationless dark matter from observations of galaxy haloes," *Nature*, vol. 370, p. 629, 1994.

[20] L. Sagunski, S. Gad-Nasr, B. Colquhoun, A. Robertson, and S. Tulin, "Velocity-dependent Self-interacting Dark Matter from Groups and Clusters of Galaxies," *JCAP*, vol. 01, p. 024, 2021.

[21] X. Li, K. Duan, W. Jiang, Z. Shen, and M. Munoz Salinas, "Recent Gamma-ray Results from DAMPE," *PoS*, vol. ICRC2019, p. 576, 2021.

[22] W. B. Atwood *et al.*, "The Large Area Telescope on the Fermi Gamma-ray Space Telescope Mission," *Astrophys. J.*, vol. 697, pp. 1071–1102, 2009.

[23] F. Aharonian *et al.*, "The h.e.s.s. survey of the inner galaxy in very high-energy gamma-rays," *Astrophys. J.*, vol. 636, pp. 777–797, 2006.

[24] G. Ambrosi *et al.*, "Direct detection of a break in the teraelectronvolt cosmic-ray spectrum of electrons and positrons," *Nature*, vol. 552, pp. 63–66, 2017.

[25] A. A. Abdo *et al.*, "Measurement of the Cosmic Ray e+ plus e- spectrum from 20 GeV to 1 TeV with the Fermi Large Area Telescope," *Phys. Rev. Lett.*, vol. 102, p. 181 101, 2009.

[26] F. Aharonian *et al.*, "The energy spectrum of cosmic-ray electrons at TeV energies," *Phys. Rev. Lett.*, vol. 101, p. 261 104, 2008.

[27] J. Aleksić *et al.*, "The major upgrade of the MAGIC telescopes, Part II: A performance study using observations of the Crab Nebula," *Astropart. Phys.*, vol. 72, pp. 76–94, 2016.

[28] J. Holder *et al.*, "The first VERITAS telescope," *Astropart. Phys.*, vol. 25, pp. 391–401, 2006.

[29] R. Battiston, "The antimatter spectrometer (AMS-02): A particle physics detector in space," *Nucl. Instrum. Meth. A*, vol. 588, A. Capone, M. De Vincenzi, F. Lucarelli, and A. Morselli, Eds., pp. 227–234, 2008.

[30] M. G. Aartsen *et al.*, "Observation of High-Energy Astrophysical Neutrinos in Three Years of IceCube Data," *Phys. Rev. Lett.*, vol. 113, p. 101 101, 2014.

[31] M. Ageron *et al.*, "ANTARES: the first undersea neutrino telescope," *Nucl. Instrum. Meth. A*, vol. 656, pp. 11–38, 2011.

[32] S. Adrián-Martínez *et al.*, "Deep sea tests of a prototype of the KM3NeT digital optical module," *Eur. Phys. J. C*, vol. 74, no. 9, p. 3056, 2014.

[33] G. Aad *et al.*, "Observation of a new particle in the search for the Standard Model Higgs boson with the ATLAS detector at the LHC," *Phys. Lett. B*, vol. 716, pp. 1–29, 2012.

[34] S. Chatrchyan *et al.*, "Observation of a New Boson at a Mass of 125 GeV with the CMS Experiment at the LHC," *Phys. Lett. B*, vol. 716, pp. 30–61, 2012.

[35] G. Aad *et al.*, "Combined Measurement of the Higgs Boson Mass in pp Collisions at $\sqrt{s} = 7$ and 8 TeV with the ATLAS and CMS Experiments," *Phys. Rev. Lett.*, vol. 114, p. 191 803, 2015.

[36] F. Abe *et al.*, "Observation of top quark production in $\bar{p}p$ collisions," *Phys. Rev. Lett.*, vol. 74, pp. 2626–2631, 1995.

[37] S. Abachi *et al.*, "Observation of the top quark," *Phys. Rev. Lett.*, vol. 74, pp. 2632–2637, 1995.

[38] "Combination of CDF and D0 Results on the Mass of the Top Quark," Mar. 2009.

[39] A. Abashian *et al.*, "The Belle Detector," *Nucl. Instrum. Meth. A*, vol. 479, pp. 117–232, 2002.

[40] L. Roszkowski, E. M. Sessolo, and S. Trojanowski, "WIMP dark matter candidates and searches—current status and future prospects," *Rept. Prog. Phys.*, vol. 81, no. 6, p. 066 201, 2018.

[41] E. Aprile, "The XENON1T Dark Matter Search Experiment," *Springer Proc. Phys.*, vol. 148, D. Cline, Ed., pp. 93–96, 2013.

[42] E. Aprile *et al.*, "Projected WIMP sensitivity of the XENONnT dark matter experiment," *JCAP*, vol. 11, p. 031, 2020.

[43] D. S. Akerib *et al.*, "First results from the LUX dark matter experiment at the Sanford Underground Research Facility," *Phys. Rev. Lett.*, vol. 112, p. 091 303, 2014.

[44] J. Aalbers *et al.*, "First Dark Matter Search Results from the LUX-ZEPLIN (LZ) Experiment," Jul. 2022.

[45] P. Agnes *et al.*, "Low-Mass Dark Matter Search with the DarkSide-50 Experiment," *Phys. Rev. Lett.*, vol. 121, no. 8, p. 081 307, 2018.

[46] P. .-A. Amaudruz *et al.*, "Design and Construction of the DEAP-3600 Dark Matter Detector," *Astropart. Phys.*, vol. 108, pp. 1–23, 2019.

[47] A. H. Abdelhameed *et al.*, "First results from the CRESST-III low-mass dark matter program," *Phys. Rev. D*, vol. 100, no. 10, p. 102 002, 2019.

[48] L. Barak *et al.*, "SENSEI: Direct-Detection Results on sub-GeV Dark Matter from a New Skipper-CCD," *Phys. Rev. Lett.*, vol. 125, no. 17, p. 171 802, 2020.

[49] A. Aguilar-Arevalo *et al.*, "Constraints on Light Dark Matter Particles Interacting with Electrons from DAMIC at SNOLAB," *Phys. Rev. Lett.*, vol. 123, no. 18, p. 181 802, 2019.

[50] Q. Arnaud *et al.*, "First germanium-based constraints on sub-MeV Dark Matter with the EDELWEISS experiment," *Phys. Rev. Lett.*, vol. 125, no. 14, p. 141 301, 2020.

[51] R. Agnese *et al.*, "Projected Sensitivity of the SuperCDMS SNOLAB experiment," *Phys. Rev. D*, vol. 95, no. 8, p. 082 002, 2017.

[52] G. Adhikari *et al.*, "Search for a Dark Matter-Induced Annual Modulation Signal in NaI(Tl) with the COSINE-100 Experiment," *Phys. Rev. Lett.*, vol. 123, no. 3, p. 031 302, 2019.

[53] G. Angloher *et al.*, "Results from the first cryogenic NaI detector for the COSINUS project," *JINST*, vol. 12, no. 11, P11007, 2017.

[54] J. Amare *et al.*, "Annual Modulation Results from Three Years Exposure of ANAIS-112," *Phys. Rev. D*, vol. 103, no. 10, p. 102 005, 2021.

[55] M. Antonello *et al.*, "The SABRE project and the SABRE Proof-of-Principle," *Eur. Phys. J. C*, vol. 79, no. 4, p. 363, 2019.

[56] R. Bernabei *et al.*, "New results from DAMA/LIBRA," *Eur. Phys. J. C*, vol. 67, pp. 39–49, 2010.

[57] E. Aprile *et al.*, "Excess electronic recoil events in XENON1T," *Phys. Rev. D*, vol. 102, no. 7, p. 072 004, 2020.

[58] E. Aprile *et al.*, "Search for New Physics in Electronic Recoil Data from XENONnT," Jul. 2022.

[59] T. Emken, C. Kouvaris, and N. G. Nielsen, "The Sun as a sub-GeV Dark Matter Accelerator," *Phys. Rev. D*, vol. 97, no. 6, p. 063 007, 2018.

[60] T. Emken, "Dark Matter in the Earth and the Sun – Simulating Underground Scatterings for the Direct Detection of Low-Mass Dark Matter," Ph.D. dissertation, Southern Denmark U., CP3-Origins, 2019.

[61] H. An, H. Nie, M. Pospelov, J. Pradler, and A. Ritz, "Solar reflection of dark matter," *Phys. Rev. D*, vol. 104, no. 10, p. 103 026, 2021.

[62] T. Emken, "Solar reflection of light dark matter with heavy mediators," *Phys. Rev. D*, vol. 105, no. 6, p. 063 020, 2022.

[63] E. Baracchini *et al.*, "PTOLEMY: A Proposal for Thermal Relic Detection of Massive Neutrinos and Directional Detection of MeV Dark Matter," Aug. 2018.

[64] F. M. Pofi, A. Apponi, G. Cavoto, C. Mariani, F. Pandolfi, I. Rago, and A. Ruocco, "Searching for Dark Matter with vertically-aligned carbon nanotubes:The ANDROMeDa project," *Nucl. Instrum. Meth. A*, vol. 1060, p. 169 072, 2024.

[65] R. Essig, M. Fernandez-Serra, J. Mardon, A. Soto, T. Volansky, and T.-T. Yu, "Direct Detection of sub-GeV Dark Matter with Semiconductor Targets," *JHEP*, vol. 05, p. 046, 2016.

[66] S. Derenzo, R. Essig, A. Massari, A. Soto, and T.-T. Yu, "Direct Detection of sub-GeV Dark Matter with Scintillating Targets," *Phys. Rev. D*, vol. 96, no. 1, p. 016 026, 2017.

[67] T. Trickle, Z. Zhang, and K. M. Zurek, "Effective field theory of dark matter direct detection with collective excitations," *Phys. Rev. D*, vol. 105, no. 1, p. 015 001, 2022.

[68] S. M. Griffin, K. Inzani, T. Trickle, Z. Zhang, and K. M. Zurek, "Extended calculation of dark matter-electron scattering in crystal targets," *Phys. Rev. D*, vol. 104, no. 9, p. 095 015, 2021.

[69] T. D. Trickle, "Direct Detection of Light Dark Matter with Electrons, Phonons, and Magnons," Ph.D. dissertation, Caltech, 2022.

[70] A. L. Fitzpatrick, W. Haxton, E. Katz, N. Lubbers, and Y. Xu, "The Effective Field Theory of Dark Matter Direct Detection," *JCAP*, vol. 02, p. 004, 2013.

[71] P. Gondolo, S. Kang, S. Scopel, and G. Tomar, "Effective theory of nuclear scattering for a WIMP of arbitrary spin," *Phys. Rev. D*, vol. 104, no. 6, p. 063 017, 2021.

[72] R. Catena, T. Emken, N. A. Spaldin, and W. Tarantino, "Atomic responses to general dark matter-electron interactions," *Phys. Rev. Res.*, vol. 2, no. 3, p. 033 195, 2020.

[73] R. K. Sachs and A. M. Wolfe, "Perturbations of a cosmological model and angular variations of the microwave background," *Astrophys. J.*, vol. 147, pp. 73–90, 1967.

[74] V. Springel, C. S. Frenk, and S. D. M. White, "The large-scale structure of the Universe," *Nature*, vol. 440, p. 1137, 2006.

[75] J. Schaye *et al.*, "The EAGLE project: Simulating the evolution and assembly of galaxies and their environments," *Mon. Not. Roy. Astron. Soc.*, vol. 446, pp. 521–554, 2015.

[76] S. Alam *et al.*, "The Eleventh and Twelfth Data Releases of the Sloan Digital Sky Survey: Final Data from SDSS-III," *Astrophys. J. Suppl.*, vol. 219, no. 1, p. 12, 2015.

[77] S. Alam *et al.*, "The clustering of galaxies in the completed SDSS-III Baryon Oscillation Spectroscopic Survey: cosmological analysis of the DR12 galaxy sample," *Mon. Not. Roy. Astron. Soc.*, vol. 470, no. 3, pp. 2617–2652, 2017.

[78] NASA/STScI; ESO WFI; Magellan/U.Arizona/D.Clowe *et al.*, "Lensing Map of 1E 0657-56,"

[79] NASA/CXC/CfA/M.Markevitch *et al.*, "X-ray Map of 1E 0657-56,"

[80] NASA/STScI; Magellan/U.Arizona/D.Clowe *et al.*, "Optical Map of 1E 0657-56,"

[81] A. Einstein, "The Foundation of the General Theory of Relativity," *Annalen Phys.*, vol. 49, no. 7, J.-P. Hsu and D. Fine, Eds., pp. 769–822, 1916.

[82] H. Katz, F. Lelli, S. S. McGaugh, A. Di Cintio, C. B. Brook, and J. M. Schombert, "Testing feedback-modified dark matter haloes with galaxy rotation curves: estimation of halo parameters and consistency with ΛCDM scaling relations," *Monthly Notices of the Royal Astronomical Society*, vol. 466, no. 2, pp. 1648–1668, Dec. 2016, ISSN: 1365-2966.

[83] E. Hubble and M. L. Humason, "The Velocity-Distance Relation among Extra-Galactic Nebulae," *Astrophys. J.*, vol. 74, pp. 43–80, 1931.

[84] F. Zwicky, "Die Rotverschiebung von extragalaktischen Nebeln," *Helv. Phys. Acta*, vol. 6, pp. 110–127, 1933.

[85] I. Newton, *Philosophiæ Naturalis Principia Mathematica*. England, 1687.

[86] Y. A. Golfand and E. P. Likhtman, "Extension of the Algebra of Poincare Group Generators and Violation of p Invariance," *JETP Lett.*, vol. 13, pp. 323–326, 1971.

[87] J.-L. Gervais and B. Sakita, "Field Theory Interpretation of Supergauges in Dual Models," *Nucl. Phys. B*, vol. 34, K. Kikkawa, M. Virasoro, and S. R. Wadia, Eds., pp. 632–639, 1971.

[88] D. V. Volkov and V. P. Akulov, "Possible universal neutrino interaction," *JETP Lett.*, vol. 16, J. Wess and V. P. Akulov, Eds., pp. 438–440, 1972.

[89] R. Catena, D. Cole, T. Emken, M. Matas, N. Spaldin, W. Tarantino, and E. Urdshals, "Dark matter-electron interactions in materials beyond the dark photon model," *JCAP*, vol. 03, p. 052, 2023.

[90] C. Abel *et al.*, "Measurement of the Permanent Electric Dipole Moment of the Neutron," *Phys. Rev. Lett.*, vol. 124, no. 8, p. 081 803, 2020.

[91] R. D. Peccei, "The Strong CP problem and axions," *Lect. Notes Phys.*, vol. 741, M. Kuster, G. Raffelt, and B. Beltran, Eds., pp. 3–17, 2008.

[92] C. Vafa and E. Witten, "Restrictions on Symmetry Breaking in Vector-Like Gauge Theories," *Nucl. Phys. B*, vol. 234, pp. 173–188, 1984.

[93] M. Gorghetto and G. Villadoro, "Topological Susceptibility and QCD Axion Mass: QED and NNLO corrections," *JHEP*, vol. 03, p. 033, 2019.

[94] C. B. Adams *et al.*, "Axion Dark Matter," in *2022 Snowmass Summer Study*, Mar. 2022.

[95] D. E. Kaplan, M. A. Luty, and K. M. Zurek, "Asymmetric Dark Matter," *Phys. Rev. D*, vol. 79, p. 115 016, 2009.

[96] L. J. Hall, K. Jedamzik, J. March-Russell, and S. M. West, "Freeze-In Production of FIMP Dark Matter," *JHEP*, vol. 03, p. 080, 2010.

[97] K. Griest and D. Seckel, "Three exceptions in the calculation of relic abundances," *Phys. Rev. D*, vol. 43, pp. 3191–3203, 1991.

[98] D. Baxter *et al.*, "Recommended conventions for reporting results from direct dark matter searches," *Eur. Phys. J. C*, vol. 81, no. 10, p. 907, 2021.

[99] R. Catena and P. Ullio, "A novel determination of the local dark matter density," *JCAP*, vol. 08, p. 004, 2010.

[100] J. Cooley, "Dark Matter direct detection of classical WIMPs," *SciPost Phys. Lect. Notes*, vol. 55, p. 1, 2022.

[101] J. D. Lewin and P. F. Smith, "Review of mathematics, numerical factors, and corrections for dark matter experiments based on elastic nuclear recoil," *Astropart. Phys.*, vol. 6, pp. 87–112, 1996.

[102] R. H. Helm, "Inelastic and Elastic Scattering of 187-Mev Electrons from Selected Even-Even Nuclei," *Phys. Rev.*, vol. 104, pp. 1466–1475, 5 Dec. 1956.

[103] E. Del Nobile, "Complete Lorentz-to-Galileo dictionary for direct dark matter detection," *Phys. Rev. D*, vol. 98, no. 12, p. 123 003, 2018.

[104] N. Anand, A. L. Fitzpatrick, and W. C. Haxton, "Weakly interacting massive particle-nucleus elastic scattering response," *Phys. Rev. C*, vol. 89, no. 6, p. 065 501, 2014.

[105] J. Fan, M. Reece, and L.-T. Wang, "Non-relativistic effective theory of dark matter direct detection," *JCAP*, vol. 1011, p. 042, 2010.

[106] A. Migdal, "Ionization of atoms accompanying α- and β-decay.," *J. Phys. USSR*, vol. 4, p. 449, 1941.

[107] M. Ibe, W. Nakano, Y. Shoji, and K. Suzuki, "Migdal Effect in Dark Matter Direct Detection Experiments," *JHEP*, vol. 03, p. 194, 2018.

[108] F. Bloch, "Über die Quantenmechanik der Elektronen in Kristallgittern," *Zeitschrift für Physik*, vol. 52, pp. 555–600,

[109] Z. Feng, X. Zhang, Y. Sakurai, Z. Wang, H. Li, and H. Hu, "Compton profile of few-layer graphene investigated by electron energy-loss spectroscopy," *Sci. Rep.*, vol. 9, no. 17313, pp. 1–5, Nov. 2019, ISSN: 2045-2322.

[110] R. Essig, A. Manalaysay, J. Mardon, P. Sorensen, and T. Volansky, "First Direct Detection Limits on sub-GeV Dark Matter from XENON10," *Phys. Rev. Lett.*, vol. 109, p. 021 301, 2012.

[111] R. Essig, T. Volansky, and T.-T. Yu, "New Constraints and Prospects for sub-GeV Dark Matter Scattering off Electrons in Xenon," *Phys. Rev. D*, vol. 96, no. 4, p. 043 017, 2017.

[112] P. Hohenberg and W. Kohn, "Inhomogeneous electron gas," *Phys. Rev.*, vol. 136, B864–B871, 3B Nov. 1964.

[113] W. Kohn and L. J. Sham, "Self-Consistent Equations Including Exchange and Correlation Effects," *Phys. Rev.*, vol. 140, A1133–A1138, 4A Nov. 1965.

[114] J. P. Perdew, K. Burke, and M. Ernzerhof, "Generalized Gradient Approximation Made Simple," *Phys. Rev. Lett.*, vol. 77, pp. 3865–3868, 18 Oct. 1996.

[115] A. Dal Corso, "A Pseudopotential Plane Waves Program (PWSCF) and some Case Studies," in *Quantum-Mechanical Ab-initio Calculation of the Properties of Crystalline Materials*, C. Pisani, Ed. Berlin, Heidelberg: Springer Berlin Heidelberg, 1996, pp. 155–178, ISBN: 978-3-642-61478-1.

[116] P. Giannozzi, S. Baroni, N. Bonini, *et al.*, "QUANTUM ESPRESSO: a modular and open-source software project for quantum simulations of materials," *Journal of Physics: Condensed Matter*, vol. 21, no. 39, p. 395 502, Sep. 2009.

[117] P. Giannozzi, O. Andreussi, T. Brumme, *et al.*, "Advanced capabilities for materials modelling with Quantum ESPRESSO," *Journal of Physics: Condensed Matter*, vol. 29, no. 46, p. 465 901, Oct. 2017.

[118] P. Giannozzi, O. Baseggio, P. Bonfà, *et al.*, "Quantum ESPRESSO toward the exascale," *The Journal of Chemical Physics*, vol. 152, no. 15, p. 154 105, 2020.

[119] E. Urdshals and M. Matas, *QEdark-EFT*, version 0.1.0, May 2021.

[120] J. Jumper, R. Evans, A. Pritzel, *et al.*, "Highly accurate protein structure prediction with alphafold," *Nature*, vol. 596, no. 7873, pp. 583–589, Aug. 2021, ISSN: 1476-4687.

[121] F. Urbina, F. Lentzos, C. Invernizzi, and S. Ekins, "Dual use of artificial-intelligence-powered drug discovery," *Nature Machine Intelligence*, vol. 4, no. 3, pp. 189–191, Mar. 2022, ISSN: 2522-5839.

[122] OpenAI, *Gpt-4 technical report*, 2023.

[123] R. Thoppilan, D. D. Freitas, J. Hall, *et al.*, *Lamda: Language models for dialog applications*, 2022.

[124] A. Q. Jiang, A. Sablayrolles, A. Mensch, *et al.*, *Mistral 7b*, 2023.

[125] Martín Abadi, Ashish Agarwal, Paul Barham, *et al.*, *TensorFlow: Large-scale machine learning on heterogeneous systems*, Software available from tensorflow.org, 2015.